

# Search for supersymmetry in diphoton final states with the CMS detector

Matthew Lawrence Joyce

June 2, 2021

## CONTENTS

1.	<i>The Standard Model of Particle Physics</i>	7
1.1	The Standard Model	7
1.2	Electroweak Symmetry Breaking	8
1.3	Problems with the SM	13
2.	<i>Supersymmetry</i>	15
3.	<i>The Large Hadron Collider</i>	16
3.1	Introduction	16
3.2	Injection Complex	16
3.3	Tunnel and Magnets	17
3.4	Luminosity	19
4.	<i>Compact Muon Solenoid</i>	21
4.1	Introduction	21
4.2	Coordinate System	22
4.3	Tracker	23
4.3.1	Pixel Detector	23
4.3.2	Strip Detector	24
4.4	Electromagnetic Calorimeter	25
4.4.1	Crystals	26
4.4.2	Barrel and Endcaps	26
4.4.3	Preshower layer	28
4.4.4	Performance	28
4.5	Hadronic Calorimeter	29
4.6	Superconducting Solenoid	30
4.7	Muon System	30
5.	<i>MIP Timing Detector (MTD)</i>	33
5.1	Introduction	33
5.2	Barrel Timing Layer	34

6.	<i>CMS Trigger System</i>	36
6.1	L1 trigger	36
6.1.1	Calorimeter trigger	36
6.1.2	Muon trigger	37
6.1.3	Global Trigger	38
6.2	High Level Trigger	38
6.3	Trigger efficiency	38
7.	<i>CMS Particle and Event Reconstruction</i>	39
7.1	Tracks	39
7.2	Calorimeter clusters	40
7.3	Object identification	40
7.3.1	Muons	40
7.3.2	Electrons	41
7.3.3	Photons	42
7.3.4	Jets	43
7.4	Missing transverse momentum	43
8.	<i>Data Analysis</i>	44
8.1	Overview	44
8.2	Data	44
8.3	Monte Carlo samples	45
8.4	Object definitions	45
8.4.1	Photons	46
8.4.2	Electrons	47
8.4.3	Muons	47
8.5	Backgrounds	47
8.5.1	Instrumental background	47
8.5.2	Electroweak background	49
8.5.3	Irreducible background	49

## LIST OF FIGURES

1.1	Illustration of the Higgs potential for $\mu^2 < 0$ . . . . .	12
1.2	Summary of content of the SM. . . . .	14
3.1	LHC interaction points . . . . .	17
3.2	Layout of LHC accelerator complex [17]. . . . .	18
3.3	Proton bunch capture onto RF bucket [7]. . . . .	19
3.4	Cross section of LHC dipole [10] . . . . .	20
3.5	Integrated luminosity delivered by the LHC to the CMS experiment each year from 2010-2018. . . . .	20
4.1	Schematic of CMS detector [24] . . . . .	21
4.2	Transverse slice of the CMS detector[8]. . . . .	22
4.3	Cross section (side) of CMS tracker prior to the Phase 1 upgrade during the year-end technical stop of 2016/2017. Each line represents a detector module while double lines indicate back-to-back strip modules. Surrounding the pixel tracker (PIXEL) is the strip detector, which is divided into the Tracker Inner Barrel (TIB), Tracker Outer Barrel (TOB), Tracker Inner Disks (TID), and Tracker Endcaps (TEC). Reprinted from Reference [13]. . . . .	24
4.4	Cross section (side) of pixel detector. The lower half , labeled "Current", shows the design prior to 2017 while the upper half, labeled "Upgrade", shows the design after the upgrade. Reprinted from Resource [12] . . . . .	25
4.5	PbWO <sub>4</sub> crystals. Left: EB crystal with APD. Right: EE crystal with VPT. Reprinted from [14] . . . . .	27
4.6	Schematic of ECAL. Reprint from [14] . . . . .	28
4.7	Longitudinal view of HCAL [2] . . . . .	30
4.8	Longitudinal slice of CMS detector while operating at 3.8-T central magnetic field. The right-hand side of the figure shows a mapping of the magnetic field lines while the left-hand side shows a mapping of the field strength. Reprint from [11] . . .	31

4.9	Cross-section of one quadrant of the CMS detector. The DTs are labeled as "MB" (Muon Barrel) and the CSCs are labelled as "ME" (Muon Endcap). The RPCs are "RB" for those in the barrel and "RE" for those in the endcap. Reprint from [25].	32
5.1	Timeline for LHC . . . . .	33
5.2	Vertices from a simulated 200 pileup event. Need to replace this with the figure from the TDR. . . . .	34
6.1	L1 trigger system. Reprint from [3] . . . . .	37
7.1	The Bremsstrahlung photons continue along a straight trajectory while the electron path is bent by the magnetic field. This results in energy deposited in the calorimeter for such electrons to be spread out along the $\phi$ -direction. . . . .	42
8.1	Two examples of GGM supersymmetry breaking processes resulting in final states containing two photons and missing transverse momentum. The T5gg model (left) shows gluinos produced from $p - p$ collisions which subsequently result in two neutralinos, each decaying to a photon and a gravitino. The T6gg model (right) shows squarks produced from $p - p$ collisions following a similar decay chain. . . . .	44
8.2	Mismeasurement of Jet3 results in an imbalance in the events transverse momentum. . . . .	48

## LIST OF TABLES

1.1	Boson fields in the SM . . . . .	8
1.2	Fermions in the SM. The first two numbers listed in the third column give the supermultiplet representation under $SU(3)_C$ and $SU(2)_L$ respectively. A <b>1</b> means that it is not charged under that group and therefore will not couple to the associated force. A <b>3</b> as the first number means that it has color charge and couples to the strong force. A <b>2</b> for the second number means that it has weak isospin and couples to the weak force. The third number gives the value of the weak isospin. Adjoint representation is specified by the presence of a bar over the number. . . . .	9
4.1	Summary of signals expected for each particle type in each sub-detector. . . . .	22
6.1	Primary HLT . . . . .	38
8.1	Data Samples . . . . .	45
8.2	Summary of loose ID photons cuts . . . . .	46
8.3	Summary of $Z\gamma\gamma \rightarrow \nu\nu\gamma\gamma$ model validation . . . . .	50

<sup>1</sup> 1. THE STANDARD MODEL OF PARTICLE PHYSICS

<sup>2</sup> 1.1 *The Standard Model*

The Standard Model (SM) of particle physics is a Lorentz-invariant quantum field theory (QFT) that describes the dynamics of elementary particles. Three critical developments leading to the formation of the SM, as described by Steven Weinberg[26], were the quark model proposed by Gell-Mann[19] and Zweig[29] in 1964, the idea of gauge symmetry by Yang and Mills[28] in 1954, and the notion of spontaneous symmetry breaking proposed by Goldstone[20] in 1961. This ultimately led to the SM in its current form as a non-Abelian gauge theory with the symmetry group

$$G_{SM} = SU(3)_C \otimes SU(2)_L \otimes U(1)_Y \quad (1.1)$$

<sup>3</sup> where  $SU(3)_C$  is responsible for strong interactions and  $SU(2)_L \otimes U(1)_Y$  is  
<sup>4</sup> responsible for unified electromagnetic and weak interactions, also known as  
<sup>5</sup> electroweak interactions.

<sup>6</sup> Associated with each of these symmetry groups is a set of massless spin-1  
<sup>7</sup> vector fields called gauge bosons. These are listed in Table 1.1 along with the  
<sup>8</sup> associated charge or generator for that group. There are eight such gauge  
<sup>9</sup> bosons in  $SU(3)_C$  called gluons  $G_\mu^{1,\dots,8}$ . There are three gauge bosons  $W_\mu^{1,2,3}$   
<sup>10</sup> in  $SU(2)_L$  and one gauge boson  $B_\mu$  in  $U(1)_Y$ . The gauge bosons mediate  
<sup>11</sup> the interactions between spin-1/2 fields  $\psi$  called fermions. At this point  
<sup>12</sup> it's worth noting that the  $W$  and  $B$  gauge fields are not observable bosons,  
<sup>13</sup> but are mixed by electroweak symmetry breaking to produce observable  
<sup>14</sup> bosons. The details of this will be covered in Section 1.2.

<sup>15</sup> There are twelve fermion fields which can be split into six lepton fields  
<sup>16</sup> and six quark fields. Both quarks and leptons are comprised of three genera-  
<sup>17</sup> tions. For quarks there are three "up-type" quarks (up  $u$ , charm  $c$ , and top  
<sup>18</sup>  $t$ ) and three "down-type" quarks (down  $d$ , strange  $s$ , and bottom  $b$ ). The  
<sup>19</sup> lepton fields are electron  $e$ , muon  $\mu$ , tau  $\tau$ , and three neutrino fields  $\nu_e$ ,  $\nu_\mu$ ,  
<sup>20</sup> and  $\nu_\tau$ . The fermion fields and their representations under  $G_{SM}$  are listed  
<sup>21</sup> in Table 1.2. Each fermion field can be expressed in terms of left and right

<sup>22</sup> chirality fields, which are represented by a doublets  $\psi_L$  in the left-handed  
<sup>23</sup> case and singlets  $\psi_R$  in the right-handed case with

$$\psi = \psi_R + \psi_L \quad (1.2)$$

$$\psi_R = \frac{1}{2}(1 + \gamma^5)\psi \quad (1.3)$$

$$\psi_L = \frac{1}{2}(1 - \gamma^5)\psi \quad (1.4)$$

<sup>24</sup> The SM also contains a complex scalar doublet field  $\phi$  called the Higgs  
<sup>25</sup> field in honor of Peter Higgs, who was among one of the physicists who  
<sup>26</sup> proposed its existence in 1964 [21].

Tab. 1.1: Boson fields in the SM

Symbol	Associated Charge	Symmetry group
$B_\mu$	weak hypercharge $Y$	$U(1)_Y$
$G_\mu^{1,\dots,8}$	color $C = (r, g, b)$	$SU(3)_C$
$W_\mu^{1,2,3}$	weak isospin $T_3$	$SU(2)_L$

The strong interaction is described by the theory of quantum chromodynamics (QCD). The Lagrangian for the QCD interaction can be written as

$$\mathcal{L}_{QCD} = \bar{\psi}(i\gamma^\mu D_\mu - m)\psi - \frac{1}{2}TrG_{\mu\nu}G^{\mu\nu} \quad (1.5)$$

<sup>27</sup> where

$$G_{\mu\nu} = \partial_\mu G_\nu - \partial_\nu G_\mu - ig_s[G_\mu, G_\nu] \quad (1.6)$$

$$D_\mu = \partial_\mu - ig_s G_\mu \quad (1.7)$$

<sup>28</sup>  $g_s$  is related to the strong coupling constant, and  $m$  is the fermion mass,  
<sup>29</sup> which in this case must be a quark since they are the only fermions with  
<sup>30</sup> color charge.

## <sup>31</sup> 1.2 Electroweak Symmetry Breaking

A crucial feature of the SM is electroweak symmetry breaking. The electroweak interaction, first proposed by Glashow, Weinberg, and Salam in the 60's, is the unified description of electromagnetic and weak interactions under the  $SU(2)_L \otimes U(1)_Y$  symmetry. The electromagnetic interaction is described by quantum electrodynamics (QED), which is an Abelian gauge

Tab. 1.2: Fermions in the SM. The first two numbers listed in the third column give the supermultiplet representation under  $SU(3)_C$  and  $SU(2)_L$  respectively. A **1** means that it is not charged under that group and therefore will not couple to the associated force. A **3** as the first number means that it has color charge and couples to the strong force. A **2** for the second number means that it has weak isospin and couples to the weak force. The third number gives the value of the weak isospin. Adjoint representation is specified by the presence of a bar over the number.

Name	Notation	Representation under $SU(3)_C \otimes SU(2)_L \otimes U(1)_Y$
Left-handed quark doublet	$\begin{pmatrix} u_L \\ d_L \end{pmatrix}, \begin{pmatrix} c_L \\ s_L \end{pmatrix}, \begin{pmatrix} t_L \\ b_L \end{pmatrix}$	(3, 2, $\frac{1}{6}$ )
Right-handed up-type quark singlet	$u_R^\dagger, c_R^\dagger, b_R^\dagger$	( $\bar{3}$ , 1, $-\frac{2}{3}$ )
Right-handed down-type quark singlet	$d_R^\dagger, s_R^\dagger, t_R^\dagger$	( $\bar{3}$ , 1, $\frac{1}{3}$ )
Left-handed lepton doublet	$\begin{pmatrix} \nu_{eL} \\ e_L \end{pmatrix}, \begin{pmatrix} \nu_{\mu L} \\ \mu_L \end{pmatrix}, \begin{pmatrix} \nu_{\tau L} \\ \tau_L \end{pmatrix}$	(1, 2, $-\frac{1}{2}$ )
Right-handed charged lepton singlet	$e_R^\dagger, \mu_R^\dagger, \tau_R^\dagger$	( $\bar{1}$ , 1, 1)

theory under the  $U(1)_{EM}$  symmetry group. The gauge boson in QED is the photon and couples to electric charge  $Q$ . The QED Lagrangian is given by

$$\mathcal{L}_{QED} = \bar{\psi}(i\gamma^\mu D_\mu - m)\psi - \frac{1}{4}F_{\mu\nu}F^{\mu\nu} \quad (1.8)$$

<sup>32</sup> where

$$F_{\mu\nu} = \partial_\mu A_\nu - \partial_\nu A_\mu \quad (1.9)$$

$$D_\mu = \partial_\mu + ieQA_\mu \quad (1.10)$$

<sup>33</sup> and  $A_\mu$  is the electromagnetic or photon field.

The Lagrangian for the unbroken  $SU(2)_L \otimes U(1)_Y$  symmetry is given by

$$\mathcal{L}_{EW} = \bar{\psi}i\gamma^\mu D_\mu\psi - Tr\frac{1}{8}W_{\mu\nu}W^{\mu\nu} - \frac{1}{4}B_{\mu\nu}B^{\mu\nu} \quad (1.11)$$

<sup>34</sup> where

$$W_{\mu\nu} = \partial_\mu W_\nu - \partial_\nu W_\mu - ig_w[W_\mu, W_\nu] \quad (1.12)$$

$$B_{\mu\nu} = \partial_\mu B_\nu - \partial_\nu B_\mu \quad (1.13)$$

with a separate fermion term for each field  $\psi_R$  and  $\psi_L$ . The covariant derivative  $D_\mu$  is given by

$$D_\mu = \partial_\mu + ig_wT_iW_\mu^i + ig_Y\frac{Y}{2}B_\mu \quad (1.14)$$

<sup>35</sup> with  $W_\mu^i$  and  $T_i$  written in terms of raising and lowering operators

$$W_\mu^\pm = \frac{1}{\sqrt{2}}(W_\mu^1 \mp W_\mu^2) \quad (1.15)$$

$$T^\pm = \frac{1}{\sqrt{2}}(T_1 \pm T_2) \quad (1.16)$$

$$W_\mu^0 = W_\mu^3 \quad (1.17)$$

$$T^0 = T_3 \quad (1.18)$$

The neutral portion of the covariant derivative  $ig_wT_3W_\mu^3 + ig_Y\frac{Y}{2}B_\mu$  must contain the electromagnetic term  $ieAQ$  for the electromagnetic interaction to be unified with the weak interaction, so the  $W_\mu^3$  and  $B_\mu$  fields need to linear combinations of the photon field  $A_\mu$  and another field  $Z_\mu$ . This relationship can be written in terms of the electroweak mixing angle  $\theta_w$ , also known as the Weinberg angle, as

$$\begin{pmatrix} A_\mu \\ Z_\mu \end{pmatrix} = \begin{pmatrix} \cos\theta_W & \sin\theta_W \\ -\sin\theta_W & \cos\theta_W \end{pmatrix} \begin{pmatrix} B_\mu \\ W_\mu^3 \end{pmatrix} \quad (1.19)$$

The weak isospin  $T_3$  and weak hypercharge  $Y$  can be related to the electric charge  $Q$  with the Gell-Mann-Nishijima formula

$$Y = 2(Q - T_3) \quad (1.20)$$

<sup>36</sup> and the coupling constants  $g_w$ ,  $g_Y$ , and  $e$  are related to the mixing angle by

$$e = g_w \cos \theta_W = g_Y \sin \theta_W \quad (1.21)$$

$$\sin \theta_W = \frac{g_Y}{\sqrt{g_w^2 + g_Y^2}} \quad (1.22)$$

$$\cos \theta_W = \frac{g_w}{\sqrt{g_w^2 + g_Y^2}} \quad (1.23)$$

At this point the  $W_\mu^{1,2,3}$  and  $B_\mu$  fields have been mixed to produce the observable fields  $W_\mu^+$ ,  $W_\mu^-$ ,  $A_\mu$ , and  $Z_\mu$ , but this is still inconsistent with experimental observations as these bosons and all of the fermions are still massless in this model. In order to generate the masses while maintaining the renormalizability of the gauge theory the symmetry needs to be spontaneously broken. This is done by the introduction of a complex scalar doublet field called the Higgs field which is expressed as

$$\phi = \begin{pmatrix} \phi^+ \\ \phi^0 \end{pmatrix} = \frac{1}{\sqrt{2}} \begin{pmatrix} \phi_1 + i\phi_2 \\ \phi_3 + i\phi_4 \end{pmatrix} \quad (1.24)$$

where the fields  $\phi_i$  are real scalar fields. The Lagrangian for the Higgs field is

$$\mathcal{L}_{Higgs} = (D_\nu \phi)^\dagger (D^\nu \phi) - V(\phi^\dagger \phi) \quad (1.25)$$

with the potential  $V(\phi^\dagger \phi)$  being given by

$$V(\phi^\dagger \phi) = \mu^2 \phi^\dagger \phi + |\lambda| (\phi^\dagger \phi)^2 \quad (1.26)$$

and the covariant derivative

$$D_\nu = \partial_\nu - \frac{i}{2} g_w W_\nu^i \sigma_i - \frac{i}{2} g_Y B_\nu \quad (1.27)$$

Since  $\mu^2 < 0$ , this potential has the shape of a sombrero as is shown in Figure 1.1. The scalar fields have some positive vacuum expectation value (VEV) satisfying

$$\phi^\dagger \phi = v = \sqrt{-\frac{\mu^2}{\lambda}} \quad (1.28)$$

at the minimum which allows us to write the ground state as

$$\phi_{ground} = \langle 0 | \phi | 0 \rangle = \frac{1}{\sqrt{2}} \begin{pmatrix} 0 \\ v \end{pmatrix} \quad (1.29)$$

Expanding the Higgs field about it's minimum as

$$\phi_{ground} \rightarrow \phi(x) = \frac{1}{\sqrt{2}} e^{i\sigma_\alpha \theta^\alpha(x)} \begin{pmatrix} 0 \\ v + h(x) \end{pmatrix}, \alpha = 1, 2, 3 \quad (1.30)$$

37 results in a massive field  $h(x)$  and three massless scalar fields, or Gold-  
38 stone bosons,  $\theta_{1,2,3}$  which represent degrees of freedom. By then trans-  
39 forming into the unitary gauge we can remove the phase factor, thereby  
40 eliminating the explicit appearance of the three Goldstone bosons in the  
41 Lagrangian. In gauging away the Goldstone bosons, the three degrees of  
42 freedom reappear as longitudinal polarization states of the  $W^+$ ,  $W^-$ , and  
43  $Z$  bosons. In other words, the  $W$  and  $Z$  bosons have become massive by  
44 "eating" the Goldstone bosons.

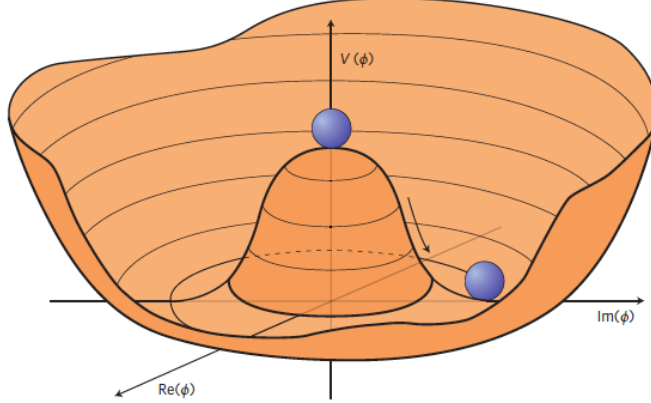


*Fig. 1.1:* The Higgs potential is shown as a function of the complex scalar field's real and imaginary parts. The balls illustrate that the stable vacuum state of nature is not located at  $\phi = 0$  because the symmetry at that point is spontaneously broken. Instead the stable vacuum state of nature is located somewhere along the circle of minimum potential. Reprint from [5]

Writing the Lagrangian in Equation 1.25 in terms of the physical  $W$  and

*Z* fields and evaluating at the VEV gives

$$\begin{aligned}\mathcal{L}_{Higgs} = & \frac{1}{2}\partial_\nu h\partial^\nu h + \frac{1}{4}g_w^2 W_\nu^+ W^{-\nu}(v+h)^2 \\ & + \frac{1}{8}\frac{g_w^2}{\cos^2\theta_W}Z_\nu Z^\nu(v+h)^2 - V[\frac{1}{2}(v+h)^2]\end{aligned}\quad (1.31)$$

<sub>45</sub> The  $v^2$  terms give the  $W$  and  $Z$  boson masses and the  $h^2$  term gives the  
<sub>46</sub> mass of the Higgs boson as

$$M_W = \frac{1}{2}g_w v \quad (1.32)$$

$$M_Z = \frac{1}{2}v\frac{g_w}{\cos\theta_W} = \frac{M_W}{\cos\theta_W} \quad (1.33)$$

$$M_H = \sqrt{2}|\mu| \quad (1.34)$$

<sub>47</sub> while the photon remains massless.

<sub>48</sub> At this point we can summarize the particle content of the SM and their  
<sub>49</sub> allowed interactions in a way that is seen in Figure 1.2.

<sub>50</sub> *1.3 Problems with the SM*

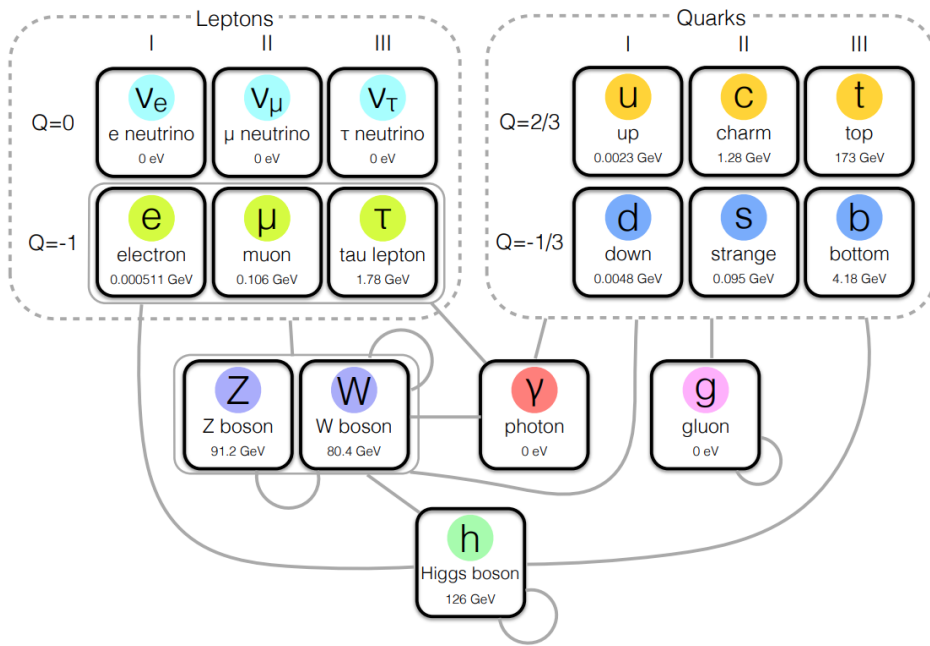


Fig. 1.2: Summary of particle content in the SM. Gray lines connecting groups of particles indicates allowed interactions. Self-coupling is indicated by a gray line connecting a particle to itself. The leptons and quarks are organized in columns corresponding to generation, which is specified at top, and rows corresponding to electric charge  $Q$ , which is listed to the left. Each particle's mass is listed beneath its name and symbol. It should be noted that neutrinos in the SM are still treated as massless leptons despite the fact that experimental evidence has established that at least two of the neutrinos are massive. Reprinted from [22]

## 2. SUPERSYMMETRY

52

### 3. THE LARGE HADRON COLLIDER

53

#### 3.1 Introduction

54 The Large Hadron Collider (LHC) is a 26.7 kilometer-long, two-ring particle  
 55 accelerator and collider located on the border of France and Switzerland at  
 56 the European Organization for Nuclear Research (CERN). During normal  
 57 operations the LHC maintains two counter-rotating beams of proton bunches  
 58 that collide at four interaction points (IP) with up to  $\sqrt{s} = 14$  TeV center  
 59 of mass energy and a luminosity of  $10^{34}\text{cm}^{-2}\text{s}^{-1}$ . The ALICE (Point 2),  
 60 ATLAS (Point 1), CMS (Point 5), and LHC-b experiments each have a  
 61 detector at one of these interaction points as scene in Figure 3.1 . The CMS  
 62 and ATLAS are general-purpose detectors while LHC-b specializes in beauty  
 63 quark studies. ALICE is a heavy-ion experiment which uses  $^{208}\text{Pb} - p$  or  
 64  $^{208}\text{Pb} - ^{208}\text{Pb}$  collisions that can also be produced by the LHC.

65

#### 3.2 Injection Complex

66 In order to bring the protons from rest up to their target collision energy  
 67 a series of accelerators, as shown in Figure 3.2, are used. The acceleration  
 68 sequence begins with the injection of hydrogen gas into a duoplasmatron.  
 69 Here a bombardment of electrons ionize the hydrogen atoms while an electric  
 70 field pushes them through the duoplasmatron cavity. The result is 100 keV  
 71 protons being passed on to a quadrupole magnet which guides them into  
 72 the aperture of a linear accelerator (LINAC2). The radio frequency (RF)  
 73 cavities in LINAC2 accelerate the protons up to 50 MeV. At this point the  
 74 protons are sent into one of four rings in the Proton Synchrotron Booster  
 75 (PSB). The PSB repeatedly accelerates the protons around a circular path  
 76 until they reach an energy of 1.4 GeV. The bunches of protons from each PSB  
 77 ring are then sequentially injected into the single-ringed Proton Synchrotron  
 78 (PS). Each bunch injected into the PS are captured by one of the "buckets"  
 79 (Figure 3.3) provided by the PS RF system which also manipulates the  
 80 bunches into the desired profile and proton density. These proton bunches  
 81 are accelerated to 25 GeV and injected into the Super Proton Synchrotron

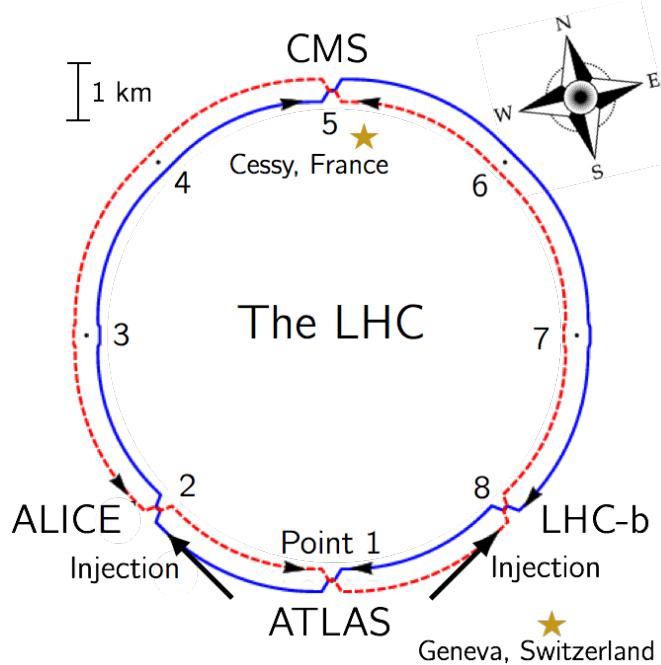


*Fig. 3.1: Interaction points of the LHC*

82 (SPS) where they are accelerated to 450 GeV. Finally the proton bunches  
 83 are injected into the LHC ring where they are accelerated to 6.5 TeV and  
 84 collided in 25 ns intervals to yield a center of mass energy of  $\sqrt{s} = 13$  TeV.

### 85           3.3 Tunnel and Magnets

86 The LHC was designed to produce collisions with up to  $\sqrt{s} = 14$  TeV. That  
 87 requires confining and guiding 7 TeV protons around the circumference of  
 88 the LHC ring. The ring is housed in a 4 meter-wide underground tunnel  
 89 that ranges in depth between 45 and 170 meters below the surface. This  
 90 tunnel was repurposed from the Large Electron-Positron (LEP) Collider  
 91 which previously occupied the space. For this reason the tunnel is not  
 92 completely circular but is instead made up of alternating curved and straight  
 93 sections of 2500 m and 530 m in length respectively. The straight sections,  
 94 labeled 1-8 in Figure 3.1, are used as either experimental facilities or sites for  
 95 hardware necessary for LHC operations such as RF cavities for momentum  
 96 cleaning, quadrupole magnets for beam focusing, and sextupole magnets for  
 97 acceleration and betatron cleaning.

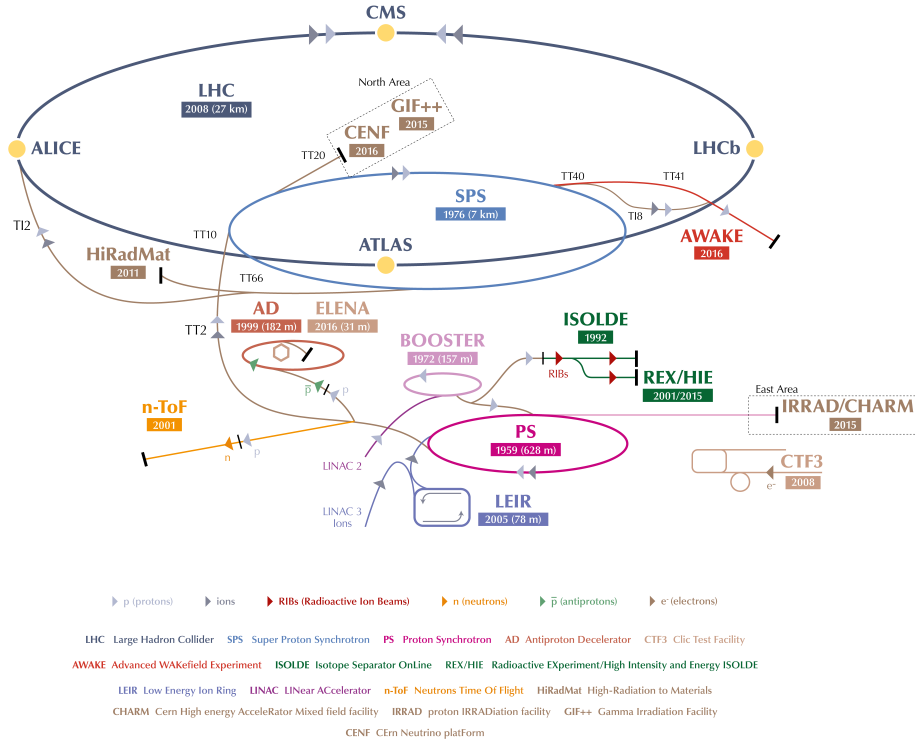


Fig. 3.2: Layout of LHC accelerator complex [17].

Steering a 7 TeV proton beam around the curved sections requires a magnetic field of 8.33 Tesla which is provided by 1223 superconducting dipole magnets cooled to 1.9 K. A cross section of the LHC dipole is shown in Figure 3.4. Supercooled liquid helium flows through the heat exchanger pipe to cool the iron yolk to a temperature of 1.9 K. Ultra high vacuum is maintained in the outer volume to provide a layer of thermal insulation between the inner volume and the outer steel casing. Inside the iron yolk is a twin bore assembly of niobium-titanium superconducting coils. Two parallel beam pipes are located within the focus of the superconducting coils. This is the ultra high vacuum region where the subatomic particles are confined as they travel around the LHC ring.

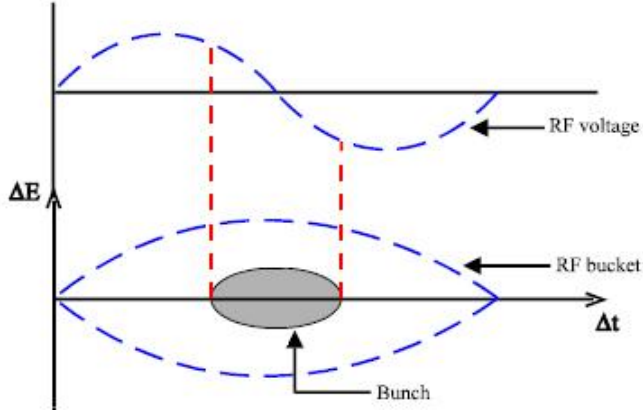


Fig. 3.3: Proton bunch capture onto RF bucket [7].

109

### 3.4 Luminosity

The number of events generated per second for specific process having cross-section  $\sigma_{event}$  is given by:

$$\frac{dN_{event}}{dt} = L\sigma_{event} \quad (3.1)$$

where  $L$  is the machine luminosity. The machine luminosity for a Gaussian beam distribution can be written in terms of the beam parameters as:

$$L = \frac{N_b^2 n_b f_{rev} \gamma_r}{4\pi \epsilon_n \beta_*} F \quad (3.2)$$

110 where  $N_b$  is particle density in each bunch,  $n_b$  is the number of bunches  
 111 in each beam,  $f_{rev}$  is the frequency of revolution, and  $\gamma_r$  is the relativistic  
 112 gamma factor. The variables  $\epsilon_n$  and  $\beta_*$  are the normalized transverse beam  
 113 emittance and the beta function at the IP respectively, while  $F$  is the geo-  
 114 metric reduction factor depending due to the beams' crossing angle at the  
 115 IP. [17]

The total number of events produced over a given amount of time would then be

$$N_{event} = \sigma_{event} \int L dt = \sigma_{event} L_{integrated}. \quad (3.3)$$

116 The integrated luminosity delivered each year to the CMS experiment is  
 117 shown in 3.5. The analysis presented here uses data collected from the 2016,  
 118 2017, and 2018 campaigns which gives a combined integrated luminosity of  
 119  $158.7 \text{ fb}^{-1}$ .

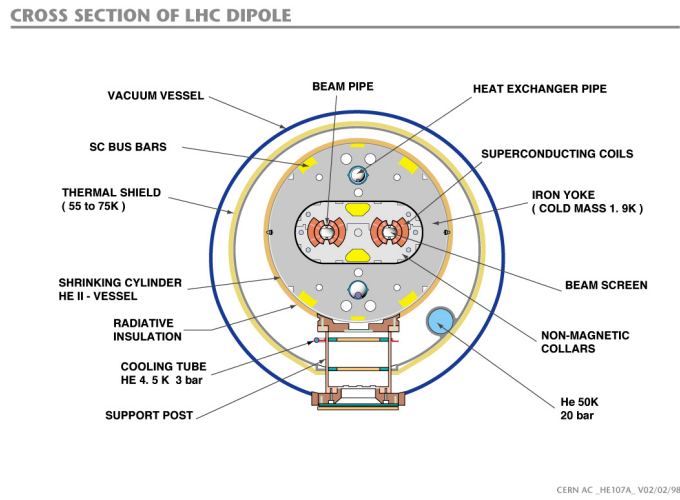


Fig. 3.4: Cross section of LHC dipole [10]

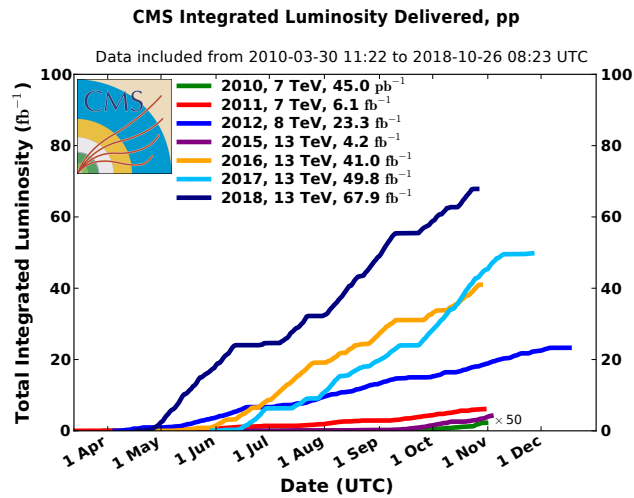
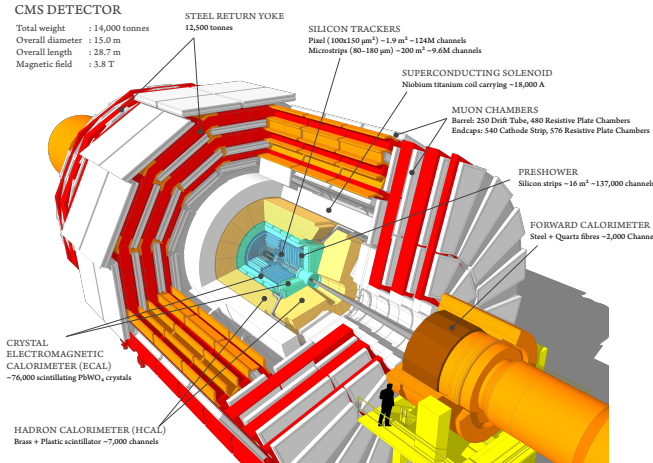


Fig. 3.5: Integrated luminosity delivered by the LHC to the CMS experiment each year from 2010-2018.

## 4. COMPACT MUON SOLENOID

### 4.1 Introduction

122 About 100 meters below the town of Cessy, France at Point 5 is the Compact  
 123 Muon Solenoid (CMS). The CMS is a general purpose detector weighing  
 124 14,000 tonnes with a length of 28.7 meters and a 15.0-meter diameter that  
 125 was designed to accurately measure the energy and momentum of particles  
 126 produced in the proton-proton or heavy-ion collisions at the LHC [14]. A  
 127 perspective view of the detector is shown in Figure 4.1. In order to get  
 128 a full picture of what is being produced by the collisions the CMS detector  
 129 must be able identify the resulting particles as well as accurately measure  
 130 their energy and momentum. For this reason the detector was designed to  
 131 be a collection of specialized sub-detectors, each of which contributes data  
 used in the reconstruction of a collision.



*Fig. 4.1: Schematic of CMS detector [24]*

133 At the heart of the CMS detector is a 3.8-Tesla magnetic field produced  
 134 by a superconducting solenoid. Inside the 6-meter diameter solenoid are

135 three layers of sub-detectors. These make up the inner detector and are, in  
 136 order from innermost to outermost, the silicon tracker, the electromagnetic  
 137 calorimeter (ECAL), and the hadronic calorimeter (HCAL). Outside the  
 138 solenoid is the muon system. A transverse slice of the detector (Figure 4.2)  
 139 shows the sub-detectors and how different types of particles interact with  
 140 them. Table 4.1 shows a summary of which sub-detectors are expected  
 141 to produce signals for different types of particles.

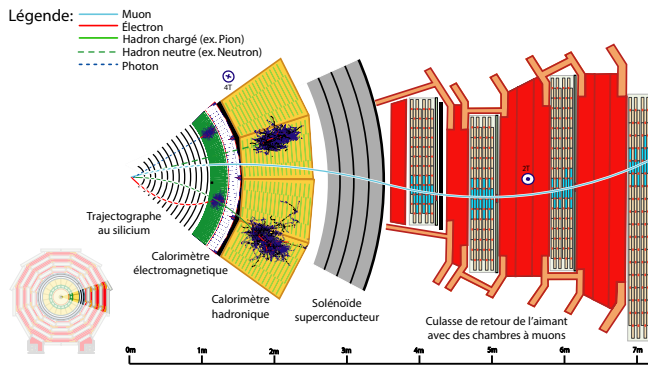


*Fig. 4.2:* Transverse slice of the CMS detector[8].

Particle	Tracker	ECAL	HCAL	Muon
Photons	No	Yes	No	No
Electrons	Yes	Yes	No	No
Hadrons (charged)	Yes	Yes	Yes	No
Hadrons (neutral)	No	No	Yes	No
Muons	Yes	Yes	Yes	Yes
Invisible ( $\nu$ , SUSY, etc)	No	No	No	No

*Tab. 4.1:* Summary of signals expected for each particle type in each sub-detector.

142

## 4.2 Coordinate System

The origin of the coordinate system used by CMS is centered at the nominal collision point in the center of the detector. A right-handed Cartesian system is used with the x-axis pointing radially inward toward the center of the LHC ring, y-axis pointing vertically upward, and the z-axis pointing tangent to

the LHC ring in the counterclockwise direction as viewed from above. CMS also uses an approximately Lorentz invariant spherical coordinate system spanned by three basis vectors. They are the transverse momentum  $p_T$ , pseudorapidity  $\eta$ , and azimuthal angle  $\phi$ . The transverse momentum and azimuthal angle translate to the Cartesian system in the following ways using the x and y-components of the linear momentum:

$$p_T = \sqrt{(p_x)^2 + (p_y)^2} \quad (4.1)$$

$$\phi = \tan^{-1} \frac{p_y}{p_x} \quad (4.2)$$

while the pseudorapidity can be translated using the polar angle  $\theta$  relative the positive z-axis as

$$\eta = -\ln[\tan \frac{\theta}{2}] \quad (4.3)$$

### 143 4.3 Tracker

144 The innermost sub-detector in CMS is the silicon tracker. The tracker is  
 145 used to reconstruct tracks and vertices of charged particles. In order to give  
 146 precise reconstruction of charged particle trajectories it needs to be position  
 147 as close as possible to the IP and have high granularity. The close proximity  
 148 to the IP requires the materials to be tolerant to the high levels of radiation  
 149 in that region. Being the innermost sub-detector it must also minimally  
 150 disturb particles as they pass through it into the other sub-detectors. These  
 151 criteria led to the design of the tracker using silicon semiconductors.

152 The silicon tracker is made up of two subsystems, an inner pixel detector  
 153 and an outer strip tracker which are oriented in a cylindrical shape with an  
 154 overall diameter of 2.4 m and length of 5.6 m centered on the interaction  
 155 point. Both subsystems consist of barrel and endcap regions which can be  
 156 seen in Figure 4.3.

#### 157 4.3.1 Pixel Detector

158 The pixel detector is the innermost subsystem in the silicon tracker and  
 159 spans the pseudorapidity range  $|\eta| < 2.5$  and is responsible for small im-  
 160 pact parameter resolution which is important for accurate reconstruction of  
 161 secondary vertices [14]. In order to produce these precise measurements a  
 162 very high granularity is required. In addition to this the proximity to the  
 163 IP means that one expects there to be high occupancy of the tracker. These  
 164 constraints are met by using pixels with a cell size of  $100 \times 150 \mu\text{m}^2$ .

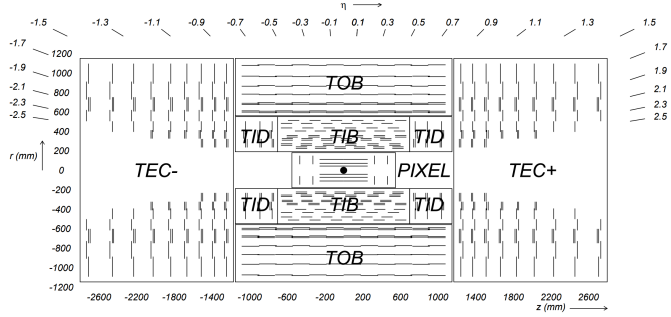


*Fig. 4.3:* Cross section (side) of CMS tracker prior to the Phase 1 upgrade during the year-end technical stop of 2016/2017. Each line represents a detector module while double lines indicate back-to-back strip modules. Surrounding the pixel tracker (PIXEL) is the strip detector, which is divided into the Tracker Inner Barrel (TIB), Tracker Outer Barrel (TOB), Tracker Inner Disks (TID), and Tracker Endcaps (TEC). Reprinted from Reference [13].

The original pixel detector was designed for operation at the nominal instantaneous luminosity of  $10^{34} \text{ cm}^{-2}\text{s}^{-1}$  with 25 ns between proton bunch crossings, resulting in on average about 25 proton-proton interactions occurring per bunch crossing or pileup [13]. During the LHC technical shutdown of 2016/17, the pixel detector underwent the scheduled Phase 1 upgrade which would allow operation at higher levels of instantaneous luminosity and pileup. Figure 4.4 shows a cross sectional view in the  $r$ - $z$  plane. Prior to 2017 there were three barrel layers and two endcap layers on each side which provide three very precise space points for each charged particle. The upgrade decreased the radius of the innermost barrel layer from 4.4 cm to 3.0 cm and added a fourth barrel layer as well as adding third endcap layer to each side. Each of the endcap layers consisted of two half-disks populated with pixel modules whereas the upgraded endcap layers were split into inner and outer rings. [12]

### 4.3.2 Strip Detector

The silicon strip detector surrounds the pixel detector and is comprised of four subsystems, the Tracker Inner Barrel (TIB), the Tracker Outer Barrel (TOB), the Tracker Inner Disks (TID), and the Tracker Endcaps (TEC), all of which can be seen in Figure 4.3 [14]. The TIB and TID both use 320  $\mu\text{m}$  thick silicon micro-strip sensors oriented along  $z$  and  $r$  respectively. The TIB has four layers while the TID is composed of three layers. This

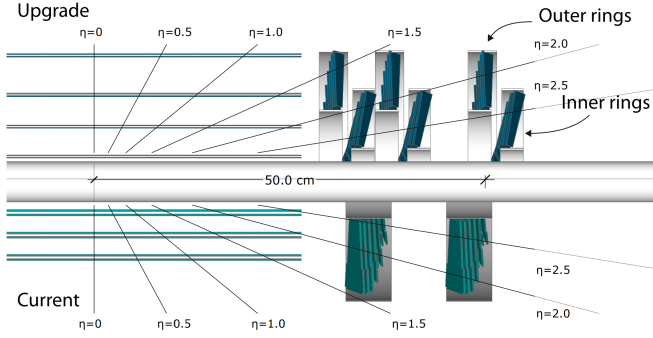


*Fig. 4.4:* Cross section (side) of pixel detector. The lower half , labeled "Current", shows the design prior to 2017 while the upper half, labeled "Upgrade", shows the design after the upgrade. Reprinted from Resource [12]

186 geometry allows the TIB and TID to combine to provide up to four  $r - \phi$   
187 measurements on charged particle trajectories.

188 Surrounding the TIB and TID is the TOB, which extends between  $z \pm 118$   
189 cm. This subsystem consists of six layers of 500  $\mu\text{m}$  thick silicon micro-strip  
190 sensors with strip pitches ranging from 122  $\mu\text{m}$  to 183  $\mu\text{m}$ , providing six  
191 more  $r - \phi$  measurements in addition to those from the TIB/TID subsystems.  
192 Beyond the  $z$  range of the TOB is the TEC. Each TEC is made up of nine  
193 disks. Each of the nine disks has up to seven concentric rings of micro-strip  
194 sensors oriented in radial strips with those on the inner four rings being  
195 320  $\mu\text{m}$  thick and the rest being 500  $\mu\text{m}$  thick, providing up to nine  $\phi$   
196 measurements for the trajectory of a charged particle.

197 To provide additional measurements of the  $z$  coordinate in the barrel and  
198  $r$  coordinate in the disks a second micro-strip detector module is mounted  
199 back-to-back with stereo angle 100 mrad in the first two layers of the TIB  
200 and TOB, the first two rings of the TID, and rings 1, 2, and 5 of the TEC.  
201 The resulting single point resolution is 230  $\mu\text{m}$  in the TIB and 530  $\mu\text{m}$  in the  
202 TOB. The layout of these subsystems ensures at least nine hits for  $|\eta| < 2.4$   
203 with at least four of hits yielding a 2D measurement.

#### 204 4.4 Electromagnetic Calorimeter

205 The electromagnetic calorimeter (ECAL) lies just outside the tracker and is a  
206 hermetic homogeneous calorimeter designed to measure the energy deposited  
207 by electrons and photons. It consists of a central barrel (EB) with 61200  
208 lead tungstate ( $\text{PbWO}_4$ ) crystals which is closed by two endcaps (EE), each

209 having 7324 crystals. Highly-relativistic charged particles passing through a  
210 crystal primarily lose energy by producing bremsstrahlung photons. Photons  
211 lose energy by producing  $e^- - e^+$  pairs. In front of each EE is a preshower  
212 (ES) detector which acts as a two-layered sampling calorimeter. The crystals  
213 in the EB are instrumented with avalanche photodiodes (APDs) while the  
214 EE crystals are instrumented with vacuum phototriodes (VPTs). The ECAL  
215 design was strongly driven to be sensitive to the di-photon decay channel  
216 of the Higgs boson. This led to the design of a calorimeter that was fast,  
217 radiation-hard, and had good spatial and energy resolution.

218                   4.4.1 Crystals

219 In order to provide a good spacial resolution it was necessary for the ECAL  
220 to have a fine granularity. The small Molier radius (22 mm) and short radia-  
221 tion length (8.9 mm) of PbWO<sub>4</sub> allows for fine granularity while maintaining  
222 good energy resolution by containing nearly all of the energy from an EM  
223 shower without the need for a restrictively thick crystal layer. The PbWO<sub>4</sub>  
224 scintillation is also fast enough that approximately 80 percent of an EM  
225 shower is produced within 25 ns, which is the also the amount of time be-  
226 tween bunch crossings at the LHC. These crystals have a Gaussian-shaped  
227 spectrum spanning from 360 nm to 570 nm with a maximum at approx-  
228 imately 440 nm. While PbWO<sub>4</sub> is relatively radiation-hard, the amount  
229 of ionizing radiation seen by the crystal leading up to the HL-LHC era of  
230 operations causes wavelength-dependent degradation in light transmission.  
231 The scintillation mechanism however is unchanged so this damage can be  
232 tracked and accounted for by injecting laser light near the peak wavelength  
233 of the emission spectrum into the crystals to monitor optical transparency.

234 Light produced in the crystal is transmitted along its length and col-  
235 lected at the rear by either an APD in the EB or a VPT in one of the EE.  
236 Light output is temperature dependent so the crystals are kept at precisely  
237 18°C at which the yield is about 4.5 photoelectrons per MeV. The EB and  
238 EB crystals, which have a tuncated pyramidal shape to match the lateral de-  
239 velopment of the shower, along with their photosensors are shown in Figure  
240 4.5.

241                   4.4.2 Barrel and Endcaps

242 The EB covers the pseudorapidity range  $|\eta| < 1.479$  and uses crystals that  
243 are 230 mm long, which corresponds to 25.8 radiation lengths. The front  
244 face of each crystal measures  $22 \times 22$  mm<sup>2</sup> while the rear face measures  $26 \times 26$

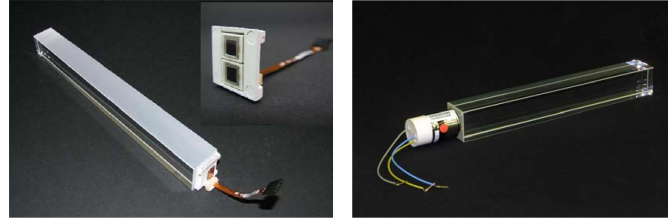


*Fig. 4.5:* PbWO<sub>4</sub> crystals. Left: EB crystal with APD. Right: EE crystal with VPT. Reprinted from [14]

mm<sup>2</sup>. These are grouped in 36 supermodules (SM), each comprised of 1700 crystals arranged in a 20×85 grid in  $\phi \times \eta$ . Each SM spans half the length of the barrel and covers 20° in  $\phi$ . On the back face of each crystal is a pair of APDs (semiconductor diodes). APDs are compact, immune to the longitudinal 3.8 T magnetic field produced by the solenoid at this location, and resistant to the radiation levels expected in the EB over a ten year period. They also have high enough gain to counter to low light yield of the crystals. All of this makes them an ideal choice for use in the EB. Each APD has an active area of 5 × 5 mm<sup>2</sup> and are operated at a gain of 50 which requires a bias voltage between 340 and 430 V. As the gain of the APDs is highly dependent on the applied bias voltage and any gain instability would translate to degradation in energy resolution, very stable power supplies are used to maintain voltages within a few tens of mV.

The EE cover the pseudorapidity range 1.497 < | $\eta$ | < 3.0. The crystals in the EE have a 28.62×28.62 mm<sup>2</sup> front face cross section and 30×30 mm<sup>2</sup> rear face cross section. Each crystal is 220 mm long which corresponds to 24.7 radiation lengths and are grouped in 5×5 units called supercrystals (SCs). Two halves, called *Dees*, make up each EE. Each Dee contains 138 SCs and 18 partial SCs which lie along the inner and outer circumference. On the back of each crystal in EE is a VPT which is a conventional photomultiplier with a single gain stage. While not as compact as the APDs used in the EB, the VPTs are a more suitable for the more hostile environment at higher  $\eta$ . Each VPT has a 25-mm diameter and approximately 280 mm<sup>2</sup> of active area. Though the VPT gain and quantum efficiency are lower than that of the APDs this is offset by the larger active area allowing for better light collection. Figure 4.6 shows the orientation of the crystals, modules, and supermodules within the ECAL. [14]

272

#### 4.4.3 Preshower layer

273 In front of each EE is a preshower (ES) detector. The main purpose of the  
 274 ES is to identify photons resulting from  $\pi^0 \rightarrow \gamma\gamma$  within the pseudorapidity  
 275 range  $1.653 < |\eta| < 2.6$ , but it also aids in the identification of electrons  
 276 against minimum ionizing particles (MIPs) and provides a spacial resolution  
 277 of 2 mm compared to the 3 mm resolution of the EB and EE. The ES acts  
 278 as a two-layered sampling calorimeter. Lead radiators make up the first  
 279 layer. These initiate electromagnetic showers from incoming electrons or  
 280 photons. The deposited energy and transverse profiles of these showers are  
 281 then measured by the silicon strip sensors which make up the second layer.

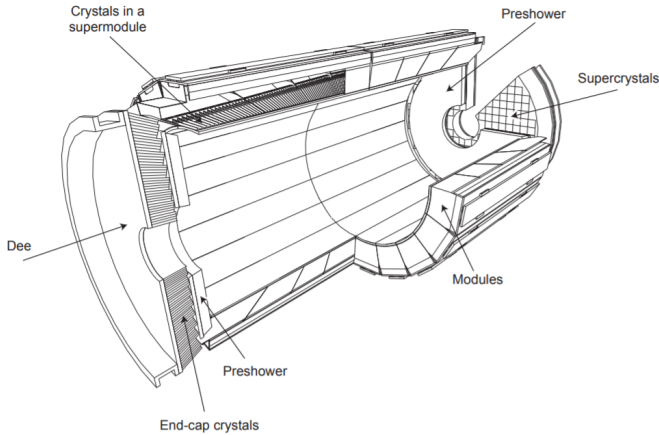


Fig. 4.6: Schematic of ECAL. Reprint from [14]

282

#### 4.4.4 Performance

The energy resolution of the ECAL can be parameterized as

$$\frac{\sigma}{E} = \frac{S}{\sqrt{E}} \oplus \frac{N}{E} \oplus C \quad (4.4)$$

283 where  $S$  is the stochastic term characterizing the size of photostatistical  
 284 fluctuations,  $N$  is the term characterizing the contributions of electronic,  
 285 digital, and pileup noise, and  $C$  is a constant which accounts for crystal  
 286 performance non-uniformity, intercalibration errors, and leakage of energy  
 287 from the back of a crystal. The values for these terms, as measured in a  
 288 beam test using 20 to 250 GeV electrons, are  $S = 0.028 \text{ GeV}^{1/2}$ ,  $N = 0.12$   
 289 GeV, and  $C = 0.003$ . [14]

290

### 4.5 Hadronic Calorimeter

291 In the space between the bore of the superconducting magnet and the ECAL  
 292 is the Hadronic Calorimeter (HCAL) [2]. The HCAL is a sampling calorime-  
 293 ter used for the measurement of hadronic jets and apparent missing trans-  
 294 verse energy resulting from neutrinos or exotic particles. It is made up of al-  
 295 ternating layers of plastic scintillator tiles and brass absorbers. EM showers  
 296 are generated by charged/neutral hadrons in the brass absorber. Charged  
 297 particles in the shower then produce scintillation light in the plastic scintil-  
 298 lator. Wavelength-shifting optical fibers embedded in the scintillator collect  
 299 and guide the scintillation light to pixelated hybrid photodiodes. A longi-  
 300 tudinal cross-section view in Figure 4.7 shows the geometric layout of the  
 301 HCAL’s barrel (HB), outer barrel (HO), endcap (HE), and forward (HF)  
 302 sections. The HB is comprised of 17 scintillator layers extending from 1.77  
 303 to 1.95 m and covers the pseudorapidity range of  $|\eta| < 1.4$ . The HO lies  
 304 outside the solenoid and is composed of only scintillating material. This  
 305 increases the interaction depth of the calorimeter system to a minimum of  
 306  $11\lambda_I$  for  $|\eta| < 1.26$  and thus reduces energy leakage. Also located inside  
 307 the solenoid are the two HE which cover pseudorapidities  $1.3 < |\eta| < 3.0$   
 308 and provide a thickness of  $10\lambda_I$ . In the forward region is the HF. This is  
 309 located 11.2 m away from the IP and covers the  $2.9 < |\eta| < 5.2$ . As the  
 310 HF is exposed to the highest levels of particle flux, it uses quartz fibers em-  
 311 bedded in steel absorbers rather than the materials used in the other parts  
 312 of the HCAL. Showers initiated by the absorbers produce Cerenkov light  
 313 in the quartz which transmits along to the fibers to photomultiplier tubes  
 314 (PMTs).

The HCAL inherently has lower energy resolution than the ECAL. A large portion of the energy from hadronic showers is deposited in the absorbers and never makes it to the scintillation material. There are also the possibilities that showers can be initiated prior to the particles reaching HCAL or a charged particle could deposit energy in the ECAL through bremsstrahlung. The combined energy resolution of the ECAL and the HCAL barrels can be parameterized as

$$\frac{\sigma}{E} = \frac{S}{\sqrt{E}} \oplus C, \quad (4.5)$$

315 where  $E$  is the energy of the incident particle. These quantities were mea-  
 316 sured in a beam test using 2 to 350 GeV/c hadrons, electrons, and muons.  
 317 The stochastic term is  $S = 0.847 \text{ GeV}^{1/2}$ , and the constant term is  $C = 0.074$   
 318 [4].

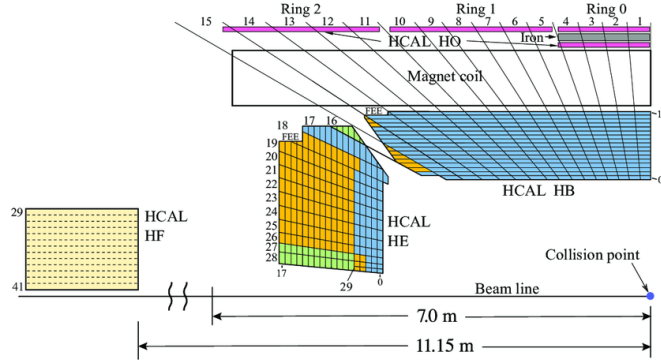


Fig. 4.7: Longitudinal view of HCAL [2]

#### 319 4.6 Superconducting Solenoid

320 In between the HCAL barrel and outer barrel is the superconducting solenoid  
 321 magnet. The magnet is 12 m long with a 6-m inner diameter and provides  
 322 the bending power necessary to precisely measure the momentum of charged  
 323 particles. While it is capable of producing a 4 T magnetic field, the magnet  
 324 is typically operated at 3.8 T. This is done to prolong the lifetime of the  
 325 magnet. The Niobium Titanium coils used to create the uniform 3.8-T  
 326 magnetic field are suspended in a vacuum cryostat and cooled by liquid helium  
 327 to a temperature of 4.5 K. The magnet has a stored energy of 2.6 GJ when  
 328 operating at full current. There are five wheels in the barrel and three  
 329 disks on each endcap that make up a 12,000 ton steel yoke which serves to  
 330 return the magnetic flux. This, along with a mapping of the calculated field  
 331 strength, can be seen in Figure 4.8. More details on the superconducting  
 332 solenoid magnet can be found at [1]

#### 333 4.7 Muon System

334 Embedded in magnet return yoke and encapsulating all of the other sub-  
 335 detectors is the muon system. The muon system is the outermost layer  
 336 because muons don't interact via the strong force and electromagnetic in-  
 337 teractions alone are not enough to stop them due to their large mass, therefore  
 338 the only particles that are capable of making it to the muon system are  
 339 muons and weakly-interacting particles such as neutrinos. The muon sys-  
 340 tem is comprised of three different types of detectors. These are drift tube  
 341 (DT) chambers, cathode strip chambers (CSC), and resistive plate chambers

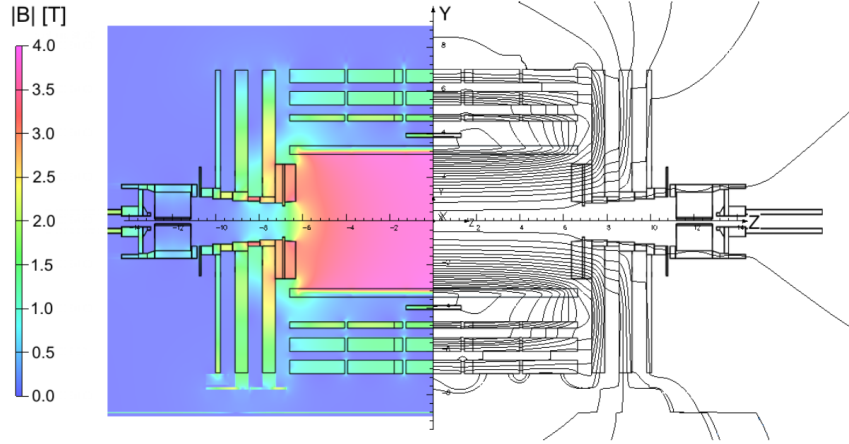


*Fig. 4.8:* Longitudinal slice of CMS detector while operating at 3.8-T central magnetic field. The right-hand side of the figure shows a mapping of the magnetic field lines while the left-hand side shows a mapping of the field strength. Reprint from [11]

(RPC). A cross-sectional view of the muon system along with the rest of the CMS detector is shown in Figure 4.9.

The DT chambers are used barrel region for  $|\eta| < 1.2$ . Each chamber is comprised of three superlayers which are made up of four staggered layers of rectangular drift cells. Each of these drift cells contains a mixture of Ar and CO<sub>2</sub> gases. An anode wire, located at the center of each tube, is made of gold-plated stainless steel and is held at 3.6 kV. The gas is ionized when a charged particle passes through and the resulting free electrons are attracted to the anode wire. As these electrons pass through the gas they cause further ionization which results in an electron avalanche. The layers of drift cells are oriented in such a way that two of the three superlayers give the muon position in the  $\phi$ -direction and one gives the position in the  $z$ -direction. The result is a spacial resolution of 77-123  $\mu\text{m}$  along the  $\phi$  direction and 133-193  $\mu\text{m}$  along the  $z$  direction for each DT chamber [15].

On the endcaps, covering the pseudorapidity range of  $0.9 < |\eta| < 2.4$ , are the CSCs. In this region there is a higher muon flux as well non-uniform magnetic fields so this portion of the muon system must have higher granularity provided by the CSCs. Each of these chambers contain panels that divide it into six staggered layers. The cathode strips are oriented along the  $r$ -direction to give position measurements in the  $\phi$ -direction while anode wires run perpendicular in between the panels to give  $r$ -direction position

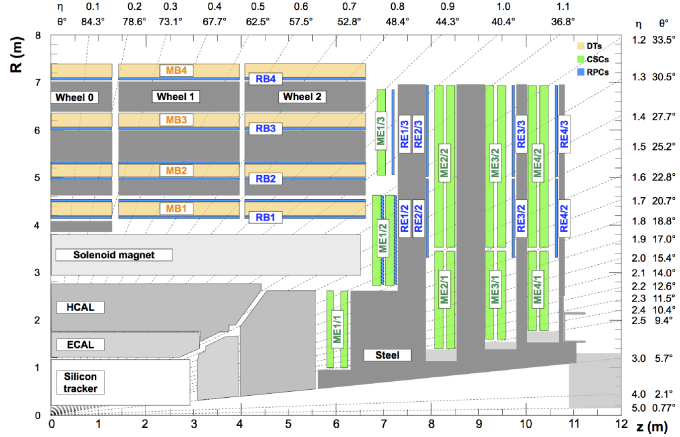


Fig. 4.9: Cross-section of one quadrant of the CMS detector. The DTs are labeled as "MB" (Muon Barrel) and the CSCs are labelled as "ME" (Muon Endcap). The RPCs are "RB" for those in the barrel and "RE" for those in the endcap. Reprint from [25].

measurements. The spacial resolution provided by the CSCs is 45-143  $\mu\text{m}$  [25].

Both the endcap and barrel regions, spanning  $|\eta| < 1.6$ , contain RPCs to provide more precise timing measurements. Each RPC is a gaseous parallel-plate detector. High voltage is applied to two large plates which have a layer of gas between them. Outside the chamber is an array of cathode strips which is used to detect electron cascades resulting from muons passing through and ionizing the gas. Where the DTs and CSCs provide precise position information, the RPCs have a very fast response time which gives a time resolution better than 3 ns [25]. This allows for the RPCs to be used as a dedicated muon trigger that can insure each muon is assigned to the correct bunch crossing.

375

## 5. MIP TIMING DETECTOR (MTD)

376

### 5.1 Introduction

377 In the coming years the LHC will be working toward upgrades that will  
 378 lead a substantial increase in luminosity. The timeline for future operations  
 379 of the LHC is shown in Figure 5.1. In 2019 the LHC entered a two-year  
 380 shutdown, Long Shutdown 2 (LS2). Upgrades of the LHC injector complex  
 381 to increase the beam brightness will take place during this shutdown. After  
 382 LS2 the LHC will enter Run 3 which will run for three years at 13-14 TeV. At  
 383 the completion of Run 3 the LHC will enter Long Shutdown 3 (LS3) which  
 384 will last approximately 2.5 years. During LS3 the optics in the interaction  
 385 region will be upgraded to produce smaller beams at the interaction point.  
 386 The completion of this upgrade will usher in the High Luminosity (HL-LHC)  
 387 era or Phase 2 of LHC operations, during which the combination of brighter  
 388 beams and a new focusing scheme at the IP allows for a potential luminosity  
 389 of  $2 \times 10^{35} \text{ cm}^{-2}\text{s}^{-1}$  at the beginning of each fill [6].

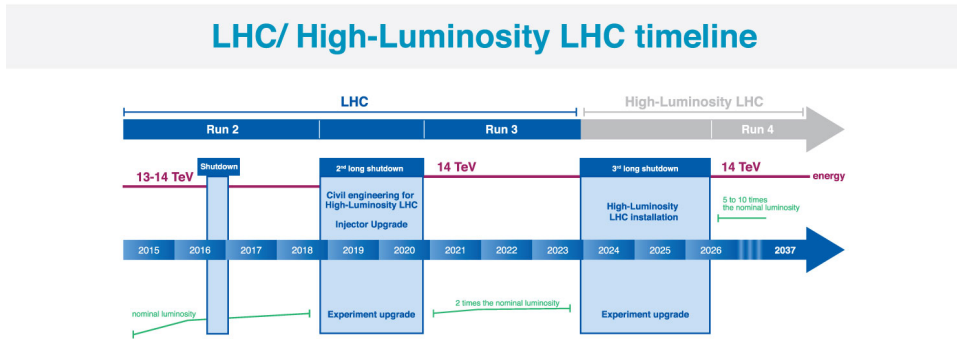
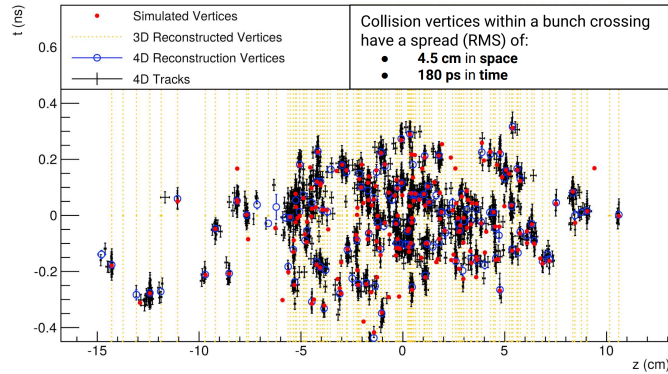


Fig. 5.1: Timeline for LHC [16]

390

The increased luminosity results in more interactions per bunch crossing or pileup. In order to limit the amount of pileup the experiments must

disentangle to more manageable levels, the nominal scenario would be operating at a stable luminosity of  $5.0 \times 10^{34} \text{ cm}^{-2} \text{ s}^{-1}$ . This would limit the pileup to an average of 140. The ultimate scenario for operations would be running at  $7.5 \times 10^{34} \text{ cm}^{-2} \text{ s}^{-1}$  which brings the average pileup up to 200. The CMS detector in its current state is not capable of dealing with  $\approx 140\text{-}200$  pileup. At this level of pileup the spacial overlaps of tracks and energy depositions would lead to a degradation in the ability to identify and reconstruct hard interactions. In order to preserve the data quality of the current CMS detector this increased pileup must be reduced to an equivalent level approximately equal to current LHC operations which is  $\sim 40$ . The collision vertices within a bunch crossing have an RMS spread of 180-200 ps in time. If the beam spot were to be sliced into consecutive snap shots of 30-40 ps then the pileup levels per snapshot would be approximately 40. The space-time reconstruction of a 200 pileup event is shown in Figure 5.2. The addition of timing information to the  $z$  position spreads apart the vertices that would otherwise have been merged together and indiscernible. In order to achieve this a detector dedicated to the precise timing of minimum ionizing particles (MIPs), the MTD, will be added to the CMS detector.



*Fig. 5.2:* Vertices from a simulated 200 pileup event. Need to replace this with the figure from the TDR.

410

## 5.2 Barrel Timing Layer

411 The Barrel Timing Layer (BTL) makes up the barrel region of the MTD.  
 412 It will provide pseudorapidity coverage up to  $|\eta| = 1.48$  with a geometric  
 413 acceptance of  $\sim 90\%$ . The BTL will be capable of detecting MIPs with a  
 414 time resolution of 30 ps at the start of Phase-2 operations and a luminosity-

<sup>415</sup> weighted time resolution of  $\sim 45$  ps when radiation damage effects are taken  
<sup>416</sup> into account.

417

## 6. CMS TRIGGER SYSTEM

418 When operating at nominal luminosity the LHC produces over 1 billion  
419 proton-proton collisions per second. Finite computing speed and storage  
420 capacity limit the rate at which CMS can record events to be about 1 kHz  
421 [9]. Decreasing the rate from 1 GHz to 1 kHz is accomplished by using a  
422 two-level trigger system to quickly decide which events will be discarded  
423 and which will be recorded. The first stage is a hardware-based Level 1 (L1)  
424 trigger and the second stage is software-based High Level Trigger (HLT).

425

### 6.1 *L1 trigger*

426 The L1 trigger decreases the rate by about six orders of magnitude from 1  
427 GHz to 100 kHz by performing rough calculations on information from the  
428 ECAL, HCAL, and muon subsystems using field-programmable gate arrays  
429 (FPGAs). The L1 trigger can be divided further into the calorimeter and  
430 muon triggers. The schematic of the L1 trigger system in Figure 6.1 shows  
431 both the calorimeter and muon triggers. The calorimeter trigger trigger  
432 uses information from the ECAL and HCAL subdetectors to construct pho-  
433 ton, electron, and jet candidates in addition to quantities such as missing  
434 transverse momentum and total hadronic activity. The muon trigger uses  
435 information from all three muon subsystems to construct muon candidates.  
436 The outputs from the calorimeter and muon triggers goes into the Global  
437 Trigger (GT) which decides which events should be recorded and which are  
438 to be discarded [27].

439

#### 6.1.1 *Calorimeter trigger*

440 Trigger Primitives (TP) are the raw inputs from the ECAL and HCAL  
441 for the calorimeter trigger. The TP, which contain information regarding  
442 the energy deposits in the calorimeters, are passed to the first layer of the  
443 calorimeter trigger. This first layer consists of several FPGA cards that  
444 receive data from several bunch crossings, but are each mapped to a section  
445 of the detector. This data is then passed on to the second layer in such a way

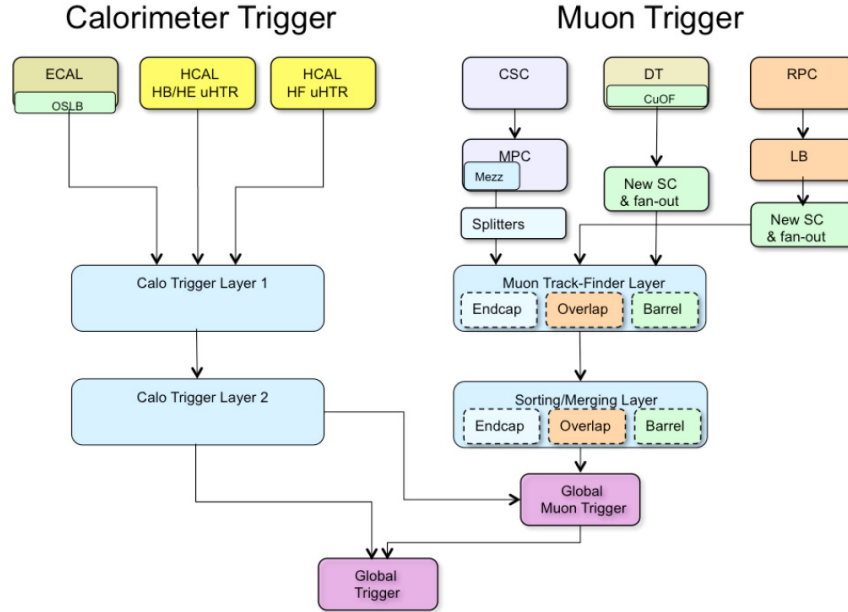


Fig. 6.1: L1 trigger system. Reprint from [3]

446 that each FPGA in this layer will receive data for the entire calorimeter for  
 447 each bunch crossing. Candidate objects are then constructed and organized  
 448 into a sorted list according to transverse momentum and passed on to the  
 449 GT and the global muon trigger.

#### 450 6.1.2 Muon trigger

451 TP for the muon trigger come from the three muon detectors, the CSCs,  
 452 DTs, and RPCs. These are then passed on to the first layer of the muon  
 453 trigger (Muon Track-Finding Layer) where the TP are combined to recon-  
 454 struct muon tracks for sections of  $\phi$  for different regions of  $|\eta|$ . The barrel  
 455 track-finder for  $|\eta| < 0.83$ , the endcap track-finder for  $|\eta| > 1.24$ , and the  
 456 overlap track-finder for  $0.83 < |\eta| < 1.24$ . This data is passed on to the  
 457 second layer where the sections of  $\phi$  are merged and subsequently passed  
 458 on to the global muon trigger where it is combined with the output from  
 459 Calo Trigger Layer 2 to compute isolation. The global muon trigger then  
 460 combines the  $\eta$  regions and passes a list of the top eight muon candidates  
 461 to the GT.

462 *6.1.3 Global Trigger*

463 Final processing of the reconstructed objects and quantities constructed by  
 464 the calorimeter and muon triggers is carried out by the GT. L1 algorithms  
 465 or "seeds" are implemented by the GT using these objects. A full set of L1  
 466 seed is called a L1 menu and can be adjusted to meet the requirements of  
 467 the CMS physics program. Each L1 seed can be given a "prescale", which is  
 468 an integer value  $N$  that can be used to reduce the rate of a particular trigger  
 469 path. This is done by only applying the trigger to one out of  $N$  events and  
 470 can be used to take advantage of the current LHC running conditions.

471 *6.2 High Level Trigger*

472 Events that are accepted by the L1 trigger are passed on to the HLT which  
 473 is based in software and is therefore capable of analyzing events with a higher  
 474 degree of sophistication. The HLT has access to information from the full  
 475 detector and implements "paths" to select events of interest from those pass-  
 476 ing the L1 trigger. Each HLT path is a set of criteria that is used to either  
 477 accept or reject an event. The full set of HLT paths is the HLT menu. Each  
 478 HLT path is "seeded" by one or more L1 seeds in order to decrease comput-  
 479 ing time. That means that a given HLT path will only be processed if the  
 480 L1 bits associated with its seed or seeds fire. Each HLT path is assigned to  
 481 a primary dataset depending on its general physics signature. In the case  
 482 of this analysis, the primary dataset used for signal events was DoubleEG  
 483 for years 2016 and 2017. This was merged into the EGamma dataset for  
 484 2018. The SingleMuon dataset was used for trigger efficiency studies. A list  
 485 of the primary HLT used for each year along with its associated primary  
 486 dataset is listed in Table 6.1. The HLT path for 2016 is different because  
 487 HLT\_DoublePhoton70 was not a part of the HLT menu until 2017.

Tab. 6.1: Primary HLT

Year	HLT path	Primary dataset
2016	HLT_DoublePhoton60	DoubleEG
2017	HLT_DoublePhoton70	DoubleEG
2018	HLT_DoublePhoton70	EGamma

488 *6.3 Trigger efficiency*

489        7. CMS PARTICLE AND EVENT RECONSTRUCTION

490        After an event is chosen to be stored by the trigger system, the output from  
491        all of the sub-detectors is saved and recorded to disk as "RAW" data. These  
492        data contain information about the response of each sub-detector, such as  
493        tracker hits and energy deposition in the calorimeters. As was mentioned  
494        in Chapter 4, shown in Table 4.1 and Figure 4.2, the CMS was designed  
495        such that each type of particle resulting from the  $pp$  collisions at the IP  
496        would leave a distinct signature in the sub-detectors. This allows for the  
497        information to be reconstructed into lists of physics object candidates such  
498        as photons, electrons, muons, etc and quantities such as missing transverse  
499        momentum. The particle flow (PF) algorithm performs this reconstruction  
500        by first building tracks and calorimeter clusters. These two elements are the  
501        inputs to the reconstruction of the aforementioned physics object candidates  
502        using a "link" algorithm.

503                  7.1    *Tracks*

504        A combinatorial track finder algorithm based on the Kalman filtering tech-  
505        nique uses the hits in the silicon tracker to reconstruct tracks of charged  
506        particles [18]. Each iteration of the algorithm is comprised of three steps:

- 507        • Seed generation: Find a seed consisting of two to three hits that is  
508        compatible with a track from a charged particle.
- 509        • Track finding: Use pattern recognition to identify any hits that are  
510        compatible with the trajectory implied by the seed generated in the  
511        first step.
- 512        • Track fitting: Determine the properties of the track, such as origin,  
513        trajectory, and transverse momentum by performing a global  $\chi^2$  fit.

514        The first iteration uses stringent requirements on the seeds and the  $\chi^2$   
515        of the track fit to pick out isolated jets which have very high purity. The  
516        hits associated with these high purity tracks are then removed to reduce the

517 combinatorial complexity for subsequent iterations. This allows successive  
518 iterations to identify less obvious tracks by progressively loosening criteria  
519 while the removal of previously associated hits mitigates the likelihood of  
520 fake tracks being built.

## 521 7.2 Calorimeter clusters

522 Calorimeter clusters are constructed using energy deposition information  
523 from the calorimeters. Clusters are formed by first identifying the seed cell  
524 (ECAL crystal or HCAL scintillating tile) that corresponds to the local  
525 maxima of an energy deposit that is above a given threshold. Neighboring  
526 cells are then aggregated to grow topological clusters if their signals are  
527 above twice the standard deviation of the level of electronic noise.

## 528 7.3 Object identification

529 At this point the tracks and calorimeter clusters are linked to form a PF  
530 block. This linkage is done with an algorithm that quantifies the likelihood  
531 that a given track and cluster were results of the same particle. As PF blocks  
532 are identified as object candidates they are removed from the collection prior  
533 to each subsequent iteration until all tracks and clusters have been assigned  
534 to a PF object candidate. The following sections will outline how each of  
535 these PF objects is identified.

### 536 7.3.1 Muons

537 Muons are the easiest particle to identify, so they are the first objects recon-  
538 structed in the CMS. PF Muons are classified in three categories depending  
539 on how their tracks are reconstructed:

- 540 • Tracker muons: Tracks reconstructed from the inner tracker having  
541  $p_T > 0.5$  GeV and  $|\vec{p}| > 2.5$  GeV that, when propagated to the muon  
542 system, match at least one hit in the muon chambers.
- 543 • Stand-alone muons: Tracks reconstructed only using hits in the muon  
544 system.
- 545 • Global muons: Stand-alone muons that coincide with a track from the  
546 inner tracker.

547 After a muon is reconstructed it is given an identification or ID based on  
548 observables such as the  $\chi^2$  of the track fit, how many hits were recorded

549 per track, or how well the tracker and stand-alone tracks matched. These  
550 IDs represent different working points (loose, medium, and tight) which  
551 correspond to increasing purity but decreasing efficiency as you move from  
552 loose toward tight.

553 **7.3.2 Electrons**

554 The next objects reconstructed in the CMS are electrons. Bremsstrahlung in  
555 the tracker layers causes substantial energy loss and changes in momentum  
556 which requires the use of a dedicated tracking algorithm. In place of the  
557 Kalman filtering technique, a Gaussian-sum filter (GSF) algorithm is used.  
558 This algorithm uses a weighted sum of Gaussian PDFs which does a bet-  
559 ter job of modeling the Bremsstrahlung effects than the Kalman filtering  
560 technique which uses a single Gaussian PDF.

561 PF ECAL clusters are regrouped by identifying a seed cluster then asso-  
562 ciating and adding clusters from Bremsstrahlung photons to form superclus-  
563 ters. The schematic in Figure 7.1 shows how the Bremsstrahlung photons  
564 are emitted in directions tangent to the trajectory of the electron. Electrons  
565 bending in the magnetic field causes spreading of PF ECAL clusters to typ-  
566 ically occur along the  $\phi$ -direction. Two approaches are used to associate  
567 the superclusters to GSF tracks. One is the ECAL-driven method, which  
568 uses superclusters with  $p_T > 4$  GeV as seeds for the GSF track finding al-  
569 gorithm. This works well for high- $p_T$  isolated electrons because the bend  
570 radius is less severe which decreases the spread of the PF ECAL clusters.  
571 This results in more of the Bremsstrahlung radiation being recovered and  
572 correctly associated with an electron candidate. The second approach is the  
573 tracker-driven method which uses tracks with  $p_T > 2$  GeV as seeds that are  
574 propagated out to the surface of the ECAL and used for clustering. This  
575 method works best with soft electrons like those in jets because it relies on  
576 the high granularity of the tracker to disentangle overlapping energy deposits  
577 in the ECAL. [23]

578 As a final step, a boosted decision tree (BDT) is used to discriminate  
579 between real and fake electrons. The BDT is given variables associated with  
580 track-cluster matching, shower shape, and tracking. The output score of  
581 the BDT is used to classify electrons into loose, medium, and tight working  
582 points which exhibit the same purity and efficiency trends as the muon  
583 working points.

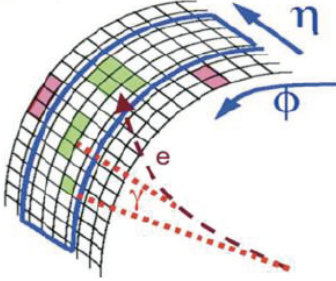


*Fig. 7.1:* The Bremsstrahlung photons continue along a straight trajectory while the electron path is bent by the magnetic field. This results in energy deposited in the calorimeter for such electrons to be spread out along the  $\phi$ -direction.

584

### 7.3.3 Photons

585 Unlike electrons, photons typically deposit most of their energy in the ECAL  
 586 without interacting with the tracker therefore their reconstruction is seeded  
 587 from ECAL superclusters that do not have any GSF tracks associated with  
 588 them. When photons interact with the tracker material they convert into  
 589 electron-positron pairs which follow bent trajectories due to the magnetic  
 590 field prior to entering the ECAL. This causes a spread of the energy deposi-  
 591 tion along the  $\phi$ -direction. The goal of the clustering algorithm for photon  
 592 reconstruction is to include all of the energy deposits of electrons resulting  
 593 from photon conversions. As with the calorimeter clustering algorithm, the  
 594 photon clustering starts by identifying a local energy maxima as a seed crys-  
 595 tal. In the EB a cluster is made up of several parallel strips of crystals  $5 \times 1$   
 596 in  $\eta \times \phi$ . The first strip has the seed crystal at its center. Neighboring strips  
 597 in the  $\phi$ -direction are added if they have energy above a threshold of 10 GeV  
 598 but less than that of the subsequent strip with a maximum of 17 strips in  
 599 a cluster. In the EE, the seed cluster is  $5 \times 5$  with adjacent  $5 \times 5$  clusters  
 600 being added if they meet the minimum energy requirement.

601 Converted and unconverted photons can be differentiated by looking at  
 602 how the energy is distributed in a supercluster. The variable  $R_9$  is used for  
 603 this purpose. It is defined as the ratio of the energy in a  $3 \times 3$  crystal array to  
 604 the energy in the entire supercluster. As the energy deposits resulting from  
 605 converted electrons is more spread out they result in a lower  $R_9$  value than  
 606 unconverted photons. A photon is candidate is considered to be unconverted  
 607 when  $R_9 > 0.93$ .

608 An important point regarding the clustering algorithm is that it does  
 609 not differentiate between showers resulting from photons and those resulting  
 610 from electrons. This allows for electron from  $Z \rightarrow ee$  events to be used as  
 611 high purity samples to study analysis inputs and for defining control regions  
 612 using electron in place of photons.

613 **7.3.4 Jets**

614 When quarks or gluons are produced they hadronize to make cone-shaped,  
 615 collimated collections of particles called jets. The jet clustering algorithm  
 616 aims to combine these particles in order to accurately measure the kine-  
 617 matics of the initial gluon or quark. The algorithm uses the two distance  
 618 parameters

$$d_{ij} = \min(k_{T_i}^{2p}, k_{T_j}^{2p}) \frac{\Delta R_{ij}^2}{R^2} \quad (7.1)$$

$$d_{iB} = k_{T_i}^{2p} \quad (7.2)$$

619 where  $d_{ij}$  is the distance between objects  $i$  and  $j$  and  $d_{iB}$  is the distance  
 620 between object  $i$  and the beam  $B$ . The transverse momentum of the object is  
 621  $k_T$ . The parameter  $p$  is set either -1, 0, or +1 to specify whether the anti- $k_T$ ,  
 622 inclusive Cambridge/Aachen, or inclusive  $k_T$  algorithm is used, respectively.  
 623 The value of  $\Delta R_{ij}^2$  is defined as  $(\eta_i - \eta_j)^2 + (\phi_i - \phi_j)^2$  and  $R$  is the distance  
 624 parameter that defines the radius of the jet.

625 his analysis uses jets reconstructed from PF candidates using the anti- $k_T$   
 626 algorithm with  $R = 0.4$ , also known as AK4PFJets or just PFJets. The  
 627 algorithm goes through the following steps:

- 628 1. The smallest values of  $d_{ij}$  and  $d_{iB}$  are computed for all objects in the  
 629 event.
- 630 2. Objects  $i$  and  $j$  are merged into a single object if  $d_{ij} < d_{iB}$ .
- 631 3. Object  $i$  is labeled as a jet and removed from the list if  $d_{iB} < d_{ij}$ .

632 Note for next time: Now talk about infrared and collinear safe. Use  
 633 Allie's thesis for guide. Look at "recent thesis" for ECAL noise on 2017  
 634 data. Should also do JEC and JER in here.

635 **7.4 Missing transverse momentum**

## 8. DATA ANALYSIS

### 8.1 Overview

638 This analysis is motivated by the GGM supersymmetry breaking scenario  
 639 in which the strong production of either gluinos or squarks result in a final  
 640 state containing two photons, jets, and missing transverse momentum. Two  
 641 example topologies are shown in Figure 8.1. If the T5gg model, each of the  
 642 produced gluinos decays to a neutralino which then decays to a photon and  
 643 a gravitino. Similarly, the T6gg model has each of the produced squarks  
 644 decays to a neutralino which then decays to a photon and a gravitino. In  
 645 both cases the gravitino escapes the CMS without detection which manifests  
 646 as missing transverse momentum.

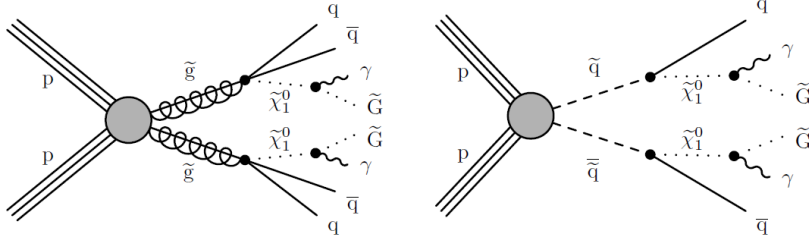


*Fig. 8.1:* Two examples of GGM supersymmetry breaking processes resulting in final states containing two photons and missing transverse momentum. The T5gg model (left) shows gluinos produced from  $p - p$  collisions which subsequently result in two neutralinos, each decaying to a photon and a gravitino. The T6gg model (right) shows squarks produced from  $p - p$  collisions following a similar decay chain.

### 8.2 Data

648 This analysis was performed using  $137 \text{ fb}^{-1}$  of data collected from the CMS  
 649 detector during the time period commonly referred to as Run 2 which spans  
 650 from 2016 to 2018. The complete list of the datasets used can be found in

651 Table 8.1. The JSON files used to identify events passing all of the CMS  
 652 offline data quality monitoring requirements are:

653 Cert\_271036\_284044\_13TeV\_23Sep2016ReReco\_Collisions16\_JSON.txt  
 654 Cert\_294927\_306462\_13TeV\_EOY2017ReReco\_Collisions17\_JSON\_v1.txt  
 655 Cert\_314472\_325175\_13TeV\_PromptReco\_Collisions18\_JSON.txt

Tab. 8.1: Data Samples

/DoubleEG/Run2016B-17July2018-ver2-v1
/DoubleEG/Run2016C-17July2018-v1
/DoubleEG/Run2016D-17July2018-v1
/DoubleEG/Run2016E-17July2018-v1
/DoubleEG/Run2016F-17July2018-v1
/DoubleEG/Run2016G-17July2018-v1
/DoubleEG/Run2016H-17July2018-v1
/DoubleEG/Run2017B-31Mar2018-v1
/DoubleEG/Run2017C-31Mar2018-v1
/DoubleEG/Run2017D-31Mar2018-v1
/DoubleEG/Run2017E-31Mar2018-v1
/DoubleEG/Run2017F-31Mar2018-v1
/EGamma/Run2018A-17Sep2018-v2
/EGamma/Run2018B-17Sep2018-v1
/EGamma/Run2018C-17Sep2018-v1
/EGamma/Run2018D-22Jan2019-v2

### 656 8.3 Monte Carlo samples

657 Monte Carlo (MC) simulation were used to validate performance of the  
 658 analysis on backgrounds, model background contributions, constructing a  
 659 multivariate discriminant, and determining signal efficiencies.

### 660 8.4 Object definitions

661 The object candidates that are identified by the reconstruction algorithms  
 662 are subject to further scrutiny in order to achieve optimal purities in the  
 663 offline analysis.

664

### 8.4.1 Photons

665 Photons are required to have  $p_T > 75$  GeV and meet the criteria prescribed  
 666 by loose ID cuts derived by the  $e/\gamma$  Physics Object Group (EGM POG).  
 667 The cut variables used to determine the photon ID are:

- 668 • H/E - The ratio of the energy deposited in the HCAL tower that is  
 669 directly behind the ECAL supercluster associated with the photon to  
 670 the energy deposited in the ECAL supercluster.
- 671 •  $\sigma_{i\eta i\eta}$  - The log-fractional weighted width of a shower in  $i\eta$ -space. This  
 672 variable is used to describe the shower shape.
- 673 • Particle Flow Charged Isolation - Sum of the  $p_T$  of charged hadrons  
 674 associated with the primary vertex within a cone of  $0.02 < \Delta R < 0.3$   
 675 of the supercluster.
- 676 • Particle Flow Neutral Isolation - Sum of the  $p_T$  of neutral hadrons  
 677 associated with the primary vertex within a cone of  $\Delta R < 0.3$  of the  
 678 supercluster.
- 679 • Particle Flow Photon Isolation - Sum of the  $p_T$  of photons within a  
 680 cone of  $\Delta R < 0.3$  of the supercluster.

681 All of the isolation variables listed above are corrected in order to remove  
 682 pileup. Table 8.2 gives a summary of the pileup-corrected requirements for a  
 683 loose ID photon. The loose ID working point has an efficiency (background  
 684 rejection) of 90.08% (86.25%) in the barrel and 90.65% (76.72%) in the end  
 685 caps. In addition to the  $p_T$  and loose ID requirements, a photon must also  
 686 pass a pixel seed veto (PSV). This means that there is no pixel seed matched  
 687 to the photon.

Tab. 8.2: Summary of loose ID photons cuts

Variable	Cut Value (Barrel)	Cut Value (Endcap)
H/E	0.04596	0.0590
$\sigma_{i\eta i\eta}$	0.0106	0.0272
Charged Iso	1.694	2.089
Neutral Iso	$24.032 + 0.01512 p_{T\gamma} + 2.259 \times 10^{-5} p_{T\gamma}^2$	$19.722 + 0.0117 p_{T\gamma} + 2.3 \times 10^{-5} p_{T\gamma}^2$
Photon Iso	$2.876 + 0.004017 p_{T\gamma}$	$4.162 + 0.0037 p_{T\gamma}$

688

### 8.4.2 Electrons

689 As mentioned earlier, the clustering algorithm doesn't differentiate between  
 690 showers from photons and those from electrons. In this analysis an electron  
 691 is defined as an object that passes all of the photon requirements except  
 692 for the PSV. Inverting the pixel seed requirement while using the same  
 693 ID criteria insures that we have orthogonal selections while minimizing the  
 694 bias potentially introduced by using control regions with electrons to model  
 695 diphoton signal regions.

696

### 8.4.3 Muons

697

## 8.5 Backgrounds

698 The sources of background in this analysis can be grouped into three cate-  
 699 gories. In order of decreasing contribution they are mismeasured hadronic  
 700 activity, electrons misidentified as photons, and standard model processes  
 701 having final states with neutrinos and two photons. In events with mul-  
 702 tiple jets, limitations on the jet energy resolution can give rise to an ap-  
 703 parent imbalance in  $p_T$  as is shown in Figure 8.2. Such events are usually  
 704 from quantum chromodynamics (QCD) processes. In these cases jets can  
 705 be misidentified as photons or there can be real photons being produced.  
 706 In both cases the result is the appearance of two photons accompanied by  
 707  $E_T^{miss}$  which mimics our signal. Given the large cross-section for QCD, this  
 708 is the most significant background in this analysis. The next background,  
 709 resulting from the misidentification of electrons as photons, comes from elec-  
 710 troweak (EWK) processes, in particular  $W\gamma$  and  $W + jets$  events where  
 711  $W \rightarrow e\nu$ . Here the neutrino contributes real  $E_T^{miss}$  while the fake photon  
 712 allows this event to fulfill the diphoton requirement. The final background  
 713 is from  $Z\gamma\gamma \rightarrow \nu\nu\gamma\gamma$  events, which exactly mimic our signal, and is modeled  
 714 using simulation as it is irreducible.

715

### 8.5.1 Instrumental background

716 The instrumental background is the contribution from events with spurious  
 717  $E_T^{miss}$  due to mismeasured hadronic activity. Since most of this background  
 718 is comprised of QCD events, it is commonly referred to as the "QCD back-  
 719 ground" and those terms are used interchangeably in this thesis. Modeling of  
 720 this background was done using the Rebalance and Smear technique while a  
 721 multivariate discriminant was constructed to improve the efficiency of iden-  
 722 tifying events with fake  $E_T^{miss}$ .

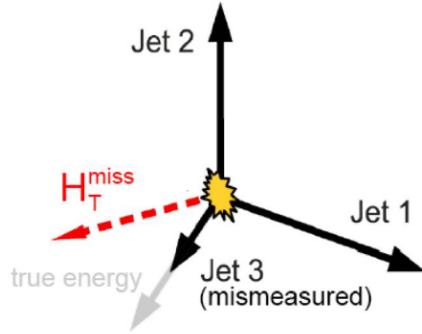


Fig. 8.2: Mismeasurement of Jet3 results in an imbalance in the events transverse momentum.

Rebalance and smear

The rebalance and smear method is used to model the spurious  $E_T^{miss}$  background. Coming soon....

726 Multivariate discriminant

727 A boosted decision tree (BDT) was used to develop a discriminating variable  
 728 for identifying events with real  $E_T^{miss}$ . The variables used are listed below.  
 729 All energy and momentum variables were normalized to the scalar sum of all  
 730 of the  $p_T$  in the event  $S_T = \sum_{\gamma,jets} |\vec{p}_T|$  in order to encourage the BDT to  
 731 focus more on how the energy and momentum was distributed in an event  
 732 rather than simply the scale of the energy or momentum.

- $S_{T_{jets}} = \sum_{jets} |\vec{p}_T|$
  - $p_{T_{jets}} = \sum_{jets} \vec{p}_T$
  - $p_{T_{\gamma\gamma}} = \vec{p}_{T_{\gamma_1}} + \vec{p}_{T_{\gamma_2}}$
  - $HardE_T^{miss} = - \sum_i \vec{p}_{T_i}$
  - $\Delta\Phi_{\gamma\gamma} = \Delta\Phi(\vec{p}_{T_{\gamma_1}}, \vec{p}_{T_{\gamma_2}})$
  - $\Delta\Phi_{min} = min[\Delta\Phi(\vec{p}_{T_{HardE_T^{miss}}}, \vec{p}_{T_{jet_i}})]$
  - $\Delta\Phi_1 = \Delta\Phi(\vec{p}_{T_{HardE_T^{miss}}}, \vec{p}_{T_{jet_1}})$

- 
- 740     •  $\Delta\Phi_2 = \Delta\Phi(\vec{p}_T_{HardE_T^{miss}}, \vec{p}_T_{jet_2})$   
 741     •  $\Delta\Phi_{\gamma\gamma, HardE_T^{miss}} = \Delta\Phi(\vec{p}_T_{HardE_T^{miss}}, \vec{p}_T_{\gamma\gamma})$   
 742     • Add the delta R stuff...

743                          8.5.2 Electroweak background

744     The electroweak background is dominated by events with  $W \rightarrow e\nu$  where  
 745     the electron is misidentified as a photon. Unlike the QCD background these  
 746     events have real  $E_T^{miss}$  due to the presence of a neutrino. The key to estimat-  
 747     ing this background is determining the rate at which electrons get incorrectly  
 748     labeled as photons in the signal region. This is done using a tag-and-probe  
 749     method where the tag is an electron (a loose ID photon that fails the PSV)  
 750     and the probe is categorized as either a photon or an electron. The result  
 751     is an electron-electron region ( $ee$ ) and an electron-photon region ( $e\gamma$ ) that  
 752     are selected from the data. As both of these regions contain  $Z \rightarrow ee$  decays,  
 753     fits are applied in each of the samples to the invariant mass spectra  $m_{ee}$  and  
 754      $m_{e\gamma}$ . The integrals of these fits are calculated over the range of the Z mass  
 755     peak to give the number of events in each category.

756                          8.5.3 Irreducible background

757     The irreducible  $Z\gamma\gamma \rightarrow \nu\nu\gamma\gamma$  background produces two photons and has  
 758     inherent  $E_T^{miss}$  via the neutrinos. There is no easy way to separate these  
 759     events from our signal so it is estimated using MC simulation. The mod-  
 760     eling of this background was tested using  $Z\gamma\gamma \rightarrow \mu\mu\gamma\gamma$  and  $Z\gamma\gamma \rightarrow ee\gamma\gamma$   
 761     events in data. Di-muon events with  $|m_{\mu\mu} - m_Z| < 15$  GeV and di-electron  
 762     events with  $|m_{ee} - m_Z| < 15$  GeV were selected and the contribution of the  
 763     muons/electrons was removed from the  $E_T^{miss}$  calculation to mimic  $Z \rightarrow \nu\nu$ .  
 764     The event selection criteria for this  $Z\gamma\gamma \rightarrow LL\gamma\gamma$  control region was

- 765         • HardMET  $> 100$  GeV  
 766         • 2 looseID photons with  $p_T > 30$  GeV  
 767         • 2 like-flavored leptons with  $p_T > 30$  GeV  
 768                 2 mediumID muons or  
 769                 2 electrons (looseID photons with a pixel seed).

The relationship

$$N_{Z \rightarrow \nu\nu} = \frac{b_{Z \rightarrow \nu\nu}}{b_{Z \rightarrow ee} + b_{Z \rightarrow \mu\mu}} (N_{Z \rightarrow ee} + N_{Z \rightarrow \mu\mu}) \quad (8.1)$$

gives an estimation for the number of  $Z\gamma\gamma \rightarrow \nu\nu\gamma\gamma$  events expected given the number of  $Z\gamma\gamma \rightarrow LL\gamma\gamma$  events observed in data where  $N_{Z \rightarrow ee}$  and  $N_{Z \rightarrow \mu\mu}$  are the number of data events passing the aforementioned selection criteria and  $b_{Z \rightarrow \nu\nu}$ ,  $b_{Z \rightarrow \mu\mu}$ , and  $b_{Z \rightarrow ee}$  are the branching ratios. The results are summarized in Table 8.3.

Tab. 8.3: Summary of  $Z\gamma\gamma \rightarrow \nu\nu\gamma\gamma$  model validation

Year	Data-driven estimation	MC estimation	$\frac{\text{data-driven}}{\text{MC}}$
2016	$30.2 \pm 12.1 \ -9.0$	$33.8 \pm 0.31$	$0.893 \pm 0.358 \ -0.267$
2017	-	-	-
2018	-	-	-

## BIBLIOGRAPHY

- [1] *The CMS electromagnetic calorimeter project: Technical Design Report.* Technical design report. CMS. CERN, Geneva, 1997.
- [2] *The CMS hadron calorimeter project: Technical Design Report.* Technical design report. CMS. CERN, Geneva, 1997.
- [3] CMS Technical Design Report for the Level-1 Trigger Upgrade. 6 2013.
- [4] S. Abdullin et al. The CMS barrel calorimeter response to particle beams from 2-GeV/c to 350-GeV/c. *Eur. Phys. J. C*, 60:359–373, 2009. [Erratum: Eur.Phys.J.C 61, 353–356 (2009)].
- [5] L. Alvarez-Gaume and J. Ellis. Eyes on a prize particle. *Nature Phys*, 7:2–3, 2011.
- [6] G. Apollinari, O. Brüning, T. Nakamoto, and Lucio Rossi. High Luminosity Large Hadron Collider HL-LHC. *CERN Yellow Rep.*, (5):1–19, 2015.
- [7] S Baird. Accelerators for pedestrians; rev. version. Technical Report AB-Note-2007-014. CERN-AB-Note-2007-014. PS-OP-Note-95-17-Rev-2. CERN-PS-OP-Note-95-17-Rev-2, CERN, Geneva, Feb 2007.
- [8] David Barney. CMS Slice. Feb 2015.
- [9] L. Cadamuro. The CMS Level-1 trigger system for LHC Run II. *JINST*, 12(03):C03021, 2017.
- [10] Jean-Luc Caron. Cross section of lhc dipole.. dipole lhc: coupe transversale. ”AC Collection. Legacy of AC. Pictures from 1992 to 2002.”, May 1998.
- [11] S Chatrchyan et al. Precise Mapping of the Magnetic Field in the CMS Barrel Yoke using Cosmic Rays. *JINST*, 5:T03021, 2010.

- [12] CMS Collaboration. CMS Technical Design Report for the Pixel Detector Upgrade. Technical Report CERN-LHCC-2012-016. CMS-TDR-11, Sep 2012. Additional contacts: Jeffrey Spalding, Fermilab, Jeffrey.Spalding@cern.ch Didier Contardo, Universite Claude Bernard-Lyon I, didier.claude.contardo@cern.ch.
- [13] CMS Collaboration. Description and performance of track and primary-vertex reconstruction with the CMS tracker. *JINST*, 9(CMS-TRK-11-001. CERN-PH-EP-2014-070. CMS-TRK-11-001):P10009. 80 p, May 2014. Comments: Replaced with published version. Added journal reference and DOI.
- [14] The CMS Collaboration. The CMS experiment at the CERN LHC. *Journal of Instrumentation*, 3(08):S08004–S08004, aug 2008.
- [15] The CMS collaboration. The performance of the CMS muon detector in proton-proton collisions at  $\sqrt{s}=7$  TeV at the LHC. *Journal of Instrumentation*, 8(11):P11002–P11002, nov 2013.
- [16] Cinzia De Melis. Timeline for the LHC and High-Luminosity LHC. Frise chronologique du LHC et du LHC haute luminosité. Oct 2015. General Photo.
- [17] Lyndon Evans and Philip Bryant. LHC machine. *Journal of Instrumentation*, 3(08):S08001–S08001, aug 2008.
- [18] R. Fruhwirth. Application of Kalman filtering to track and vertex fitting. *Nucl. Instrum. Meth. A*, 262:444–450, 1987.
- [19] Murray Gell-Mann. A Schematic Model of Baryons and Mesons. *Phys. Lett.*, 8:214–215, 1964.
- [20] J. Goldstone. Field Theories with Superconductor Solutions. *Nuovo Cim.*, 19:154–164, 1961.
- [21] Peter W. Higgs. Broken Symmetries and the Masses of Gauge Bosons. *Phys. Rev. Lett.*, 13:508–509, 1964.
- [22] Yutaro Iiyama. *Search for Supersymmetry in pp Collisions at  $\sqrt{s} = 8$  TeV with a Photon, Lepton, and Missing Transverse Energy*. PhD thesis, Carnegie Mellon U., 2 2015.
- [23] Jonas Rembser. CMS Electron and Photon Performance at 13 TeV. *J. Phys.: Conf. Ser.*, 1162(1):012008. 8 p, 2019.

- [24] Tai Sakuma and Thomas McCauley. Detector and event visualization with SketchUp at the CMS experiment. *Journal of Physics: Conference Series*, 513(2):022032, jun 2014.
- [25] A.M. Sirunyan et al. Performance of the CMS muon detector and muon reconstruction with proton-proton collisions at  $\sqrt{s}=13$  TeV. *Journal of Instrumentation*, 13(06):P06015–P06015, jun 2018.
- [26] Steven Weinberg. The Making of the standard model. *Eur. Phys. J. C*, 34:5–13, 2004.
- [27] J. Wittmann, B. Arnold, H. Bergauer, M. Jeitler, T. Matsushita, D. Rabady, B. Rahbaran, and C.-E. Wulz. The upgrade of the CMS global trigger. *Journal of Instrumentation*, 11(02):C02029–C02029, feb 2016.
- [28] Chen-Ning Yang and Robert L. Mills. Conservation of Isotopic Spin and Isotopic Gauge Invariance. *Phys. Rev.*, 96:191–195, 1954.
- [29] G. Zweig. *An SU(3) model for strong interaction symmetry and its breaking. Version 2.* 2 1964.